nuclear fusion
IAEA

PAPER • OPEN ACCESS

A compact fusion reactor based on the staged compression of a field reversed configuration

To cite this article: John Slough 2025 *Nucl. Fusion* **65** 106019

View the article online for updates and enhancements.

You may also like

- THE PHYSICS OF THE FAR-INFRARED–RADIO CORRELATION. I. CALORIMETRY, CONSPIRACY, AND IMPLICATIONS
Brian C. Lacki, Todd A. Thompson and Eliot Quataert
- On-chip human lymph node stromal network for evaluating dendritic cell and T-cell trafficking
Brian J Kwee, Mona Mansouri, Adovi Akue et al.
- Enhanced plasma performance in C-2W advanced beam-driven field-reversed configuration experiments
H. Gota, A. Smirnov, M.W. Binderbauer et al.

This content was downloaded from IP address 172.56.106.63 on 15/09/2025 at 16:37

OPEN ACCESS
IOP Publishing | International Atomic Energy Agency
Nuclear Fusion
Nucl. Fusion **65** (2025) 106019 (26pp)
https://doi.org/10.1088/1741-4326/ae034d

A compact fusion reactor based on the staged compression of a field reversed configuration

John Slough

MSNW LLC, Bellevue, WA 98008, United States of America

E-mail: sloughj@msnwllc.com

Received 26 June 2025, revised 12 August 2025
Accepted for publication 4 September 2025
Published 15 September 2025

Abstract

A new methodology for achieving the formation and compressional heating of a field reversed configuration (FRC) plasmoid has been investigated both theoretically and experimentally at the University of Washington and MSNW. This approach, based on previous FRC empirical scaling, is expected to achieve fusion gain as large as 10. For the FRC, the fusion gain, $G \sim \varphi_p \cdot B_e^2$ where φ_p is the FRC poloidal flux and B_e the confining axial magnetic field. G is essentially independent of the FRC radial scale making feasible a small, compact reactor. The necessary φ_p (>60 mWb) is achieved by employing a large formation chamber (∼0.8 m radius) combined with the requisite axial magnetic field reversal time ($E_\theta \sim 20$ kV m^{-1}) for generating a high initial temperature ($T_i > 1$ keV) FRC. By employing the dynamic formation procedure, the FRC is accelerated to ∼100–150 km s^{-1}. This subsonic velocity is maintained as the FRC is translated through a series of cylindrical coils of decreasing radius but of sufficient length ($>L_{FRC}$) and number (∼10) to produce essentially an isentropic and adiabatic radial wall-compression of the equilibrium FRC. The final stage is a 12 cm diameter, 3–6 m long confinement and burn chamber with a vacuum field of 7–9 T produced by external solenoidal coils inside the flux conserving cylinder. The vacuum field is compressed by the FRC on insertion to 35 T resulting in fusion gain conditions for the 2–5 ms transit. The large ratio of FRC to inner wall radius (0.85) substantially lowers the FRC edge pressure thereby greatly reducing both particle and thermal losses. The resulting D–T fusion yield for the 3.5 MJ FRC is 20–40 MJ/pulse. The final ejection and expansion of the FRC into a large, low field mirror chamber provides a mechanism for FRC energy recovery. The experimental justification and the physics basis for the entire process from formation through burn of the Compact FRC Fusion Reactor concept is presented.

Keywords: field reversed configuration, FRC, staged magnetic compression, energy recovery, fusion gain, FRC stability, wall compression

Original content from this work may be used under the terms of the Creative Commons Attribution 4.0 licence. Any further distribution of this work must maintain attribution to the author(s) and the title of the work, journal citation and DOI.

1. Introduction

To be competitive with fission and other energy sources, fusion energy production for electrical power must significantly reduce scale, time, and cost. For FRCs the fusion power peak density scales as B^2. It is therefore imperative to develop devices that can operate in a very high β regime able to maximize pressure with the B^2 scaling. The field reversedconfiguration (FRC) has a simple cylindrical magnetic coil geometry and high plasma β along with several attractive and unique engineering features for development of a simpler and more economical fusion reactor. Attractive engineering features of an FRC based fusion reactor would include: (1) A simply connected vacuum system enhancing design, access, and maintenance. (2) The absence of toroidal field coils making periodic blanket and reactor Plasma Facing Components replacement or repair feasible. (3) Magnetic confinement is provided by cylindrical solenoidal coils which are structurally much easier to design and construct while also providing for the highest magnetic fields. (4) A linear reactor which allows for efficient energy extraction as well as impurity control via plasma outflow along open field lines to large, remote divertor regions. (5) Minimal damage from off-normal plasma termination due to the simple linear geometry. (6) The ability to form and heat the FRC remotely in a far less demanding environment than that within the fusion burn chamber, and a significant advantage for the concept to be considered here. This arrangement also avoids the need for large port access for heating and sustainment in the reactor. Additionally, it simplifies the placement of the breeding blanket and maximizes its coverage. (7) Utilizing pulsed operation with efficient energy recovery offers a straightforward method to regulate power output in accordance with load demand, while maintaining fusion gain and overall efficiency. (8) Owing to the inherently high energy density of the FRC, it is possible, if not imperative, to build smaller-sized, more affordable reactors, such as the Compact FRC Fusion Reactor (CFR2) concept to be presented here. Considering these advantages, each phase of the experimental development of the CFR2 is anticipated to require less time as well as less costly.

It is essential that the evaluation metrics for the various methodologies being pursued for each FRC reactor concept should be determined based on the incorporation of the aforementioned advantages. The intent of this paper is to present experimental data and theoretical analysis to substantiate that the CFR2 approach can feasibly integrate all these benefits.

Achieving success in the formation of stable, high-temperature, well-confined FRCs would signify a transformative change in fusion power development. Nevertheless, FRC based fusion faces substantial challenges for viability due primarily to stability issues and confinement scaling. As will be discussed, these concerns significantly restrict the operational space for attaining fusion gain. The primary physics challenges associated with FRCs must include ensuring stability from formation through burn and achieving the required confinement to secure sufficient fusion gain for an economical and safe reactor, and to accomplish this without undermining the unique attributes of FRCs. The subsequent sections will demonstrate that these requirements can be fulfilled through a method for generating adequate FRC poloidal flux to provide necessary confinement, and a process for efficiently heating the FRC—particularly the ions—to maintain stability from formation through burn.

These criteria can be successfully addressed by the staged compression method which is based on previous research concerning the formation, transport, and stability of FRCs [1–8]. Prior to detailing this approach, it is essential to understand what are the underlying assumptions with regard to both the confinement scaling and region of stability for the FRC, and how they were arrived at.

2. Background

2.1. FRC flux and particle confinement

In the context of the FRC, poloidal flux, φ_p is of paramount importance as it represents the sole confining magnetic field. Consequently, in nearly all FRC devices, both particle and energy confinement times are found to be proportional to the initial flux within the FRC. There is, however, no apparent reason for the flux decay rate to be analogous to the particle loss rate displaying a similar parameter dependence [4]. The reason to expect some discrepancy arises from the differing locations and conditions under which flux and particle loss occur. Flux loss should reflect conditions at the field null, where gradients of the field and pressure are minimal, whereas particle loss occurs at the separatrix, marked by steep gradients caused by the rapid depletion of pressure and particles escaping along the 'open' field lines. It is found that there is a rationale behind this confinement correspondence, though a comprehensive explanation and discussion will be deferred to later in section 4.3.

Particle loss constitutes the primary energy loss channel for the FRC, whereas the decay of poloidal flux has been the principal factor in limiting the operational lifespan. However, in a series of groundbreaking experiments conducted at Tri Alpha Energy Technologies (TAE), it was demonstrated that FRC could be sustained through the injection of high-energy neutral beams [8]. This sustainment differs markedly from the neutral beam current drive observed in tokamaks. In tokamaks, characterized by a dominant toroidal field, the toroidal current responsible for the poloidal field exhibits a resistivity that approximates classical. Conversely, in FRCs, the current is diamagnetic, and the cross-field resistivity appears quite anomalous. Through strategic injection of neutral beams, it is feasible to maintain the plasma pressure profile, thereby sustaining the diamagnetic current. Given the negligible magnetic field at the null point, the beam does not induce a significant change in pressure there over time and does not produce an increase in φ_p. Consequently, the initial equilibrium poloidal flux is best established via the FRC field reversed formation methodology. Although evidence suggests that sufficiently powerful beams can generate an FRC [9], the resistivity remains anomalous, and the resultant flux is

minimal relative to the experimental scale and required beam power.

It is therefore assumed that a field reversed theta pinch (FRTP) technique will be employed to generate the FRC flux as it has been shown to be the one method that can produce a stable, well-confined FRC at high flux. Consequently, this will affect both the scale of the FRC formation system as well as the fill pressure and coil loop voltage that must be employed to produce an appropriate FRC for fusion gain.

It should be noted that there have been few direct measurements of the FRC poloidal flux in past FRC experiments. This is primarily due to the high β nature of the FRC and the relatively small magnitude of the poloidal fields (0–0.3 T). In addition, probe measurements that have been made cause major disturbances in the FRC, shorting out what appears to be large internal electric fields, quenching plasma temperature and ultimately destroying confinement. The fields are small and error bars large. Inverting density profiles are indirect measurements of the flux and are consistent with a rigid rotor (RR) profile inside the separatrix, although, as will be seen, assuming this profile in all cases could possibly cause errors as well as potentially inaccurate inferences of increased flux from either neutral beams [10] or FRC injection [11]. The poloidal flux is typically made by inference from external plasma radius and magnetic field measurements, assuming the average beta condition [1] holds along with the assumption of a RR poloidal flux profile $\varphi_{RR} = r_s{}^3/r_c{\cdot}B_e$, where B_e is the magnetic field external to the FRC [2]. The average beta condition, $<\beta> 1 - {}^1/_2(r_s/r_c)^2$, where r_s is the FRC separatrix radius and r_c the coil radius, was derived with the assumption that the FRC resides in a hollow cylindrical flux-conserving coil where the flux is uniformly constant throughout coil length, and which also extends well beyond the ends of the FRC. This is not typically the case for these experiments. A change in the coil radius at the ends of the confining coil, or a change in the flux (a mirror field) significantly alter the assumed poloidal flux from its true value.

Evaluating the poloidal flux is crucial for assessing the FRC's stability and confinement. A quantitative examination of the magnitude of the error when the FRC is confined in a spatially non-constant flux conserver (e.g. magnetic mirror field) was undertaken. A series of 2D MHD calculations were conducted with varying field strengths in the end region axially outside the FRC. It can be seen in figure 1 that as the mirror ratio increases, the FRC separatrix radius expands and its profile becomes more hollow (larger region of low field near the null). The FRC flux estimation based on the FRC excluded flux radius, $r_{\Delta\varphi}$ being approximately equal to r_s, the average β condition, and the assumption of a RR profile, significantly overestimates the true FRC poloidal flux as shown in figure 2. The error is significant for even small mirror ratios.

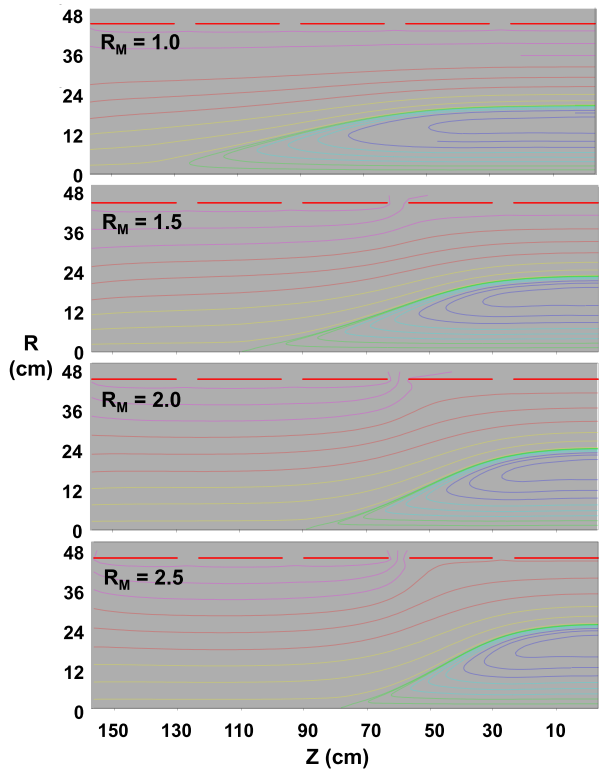

Figure 1. Plots equilibrium external and FRC magnetic field lines from 2D MHD calculations where the magnetic mirror ratio R_M is that of the magnetic flux in the end region to that at the FRC midplane ($z = 0$).

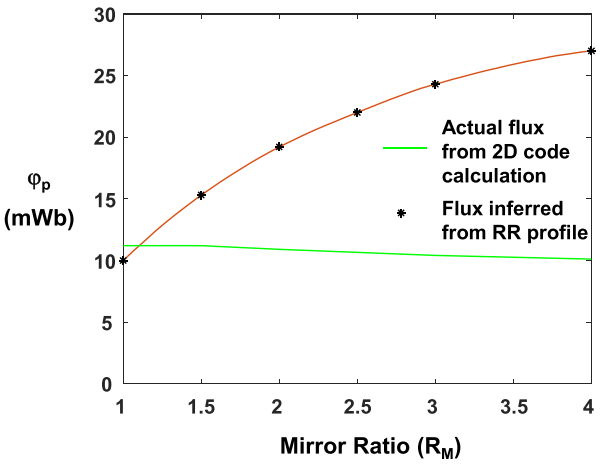

Figure 2. FRC poloidal flux as a function of the mirror ratio from 2D MHD calculations compared to that inferred from FRC excluded flux radius measurements assuming a Rigid Rotor (RR) profile that satisfies the average β condition for $R_M = 1$ (no mirror).

2.1.1. FRC confinement scaling. Measurements of FRC lifetimes have been made by several groups over the early years of FRC research [4, 12–16]. The effort culminated in the Large s Experiment (LSX) in the early 1990s. The LSX data comprised both the largest and the best confined ($n{\cdot}\tau_N \sim 10^{18}$ m^{-3} s) FRCs produced to date and extended the empirical scaling results obtained in other devices. The measured FRC lifetimes were obtained at values of s (ratio of radial scale length to ion gyroradius [13]) that were beyond what was thought to be the tilt mode stability boundary of $s/\varepsilon \sim 0.5$. Here ε is the FRC aspect ratio ($l_s/2r_s$). The LSX experiment was prematurely terminated by the cancelation of all alternate fusion concepts by the U.S. DOE leaving

unresolved the possibility of further advancements and a definitive determination of the kinetic stability boundary for FRC.

Currently, the leading edge of FRC research in now conducted with private funding, notably TAE Technologies (TAE) and Helion Energy (HE). These efforts, however, are primarily focused on achieving fusion using advanced fuel cycles (P-^{11}B and D-^{3}He, respectively). Due to the nature of privately funded research, there have been no reported studies that extend the fundamental transport and confinement properties of the FRC over the broad range of conditions at a scale as large or larger than LSX. Thus, the scaling to be adopted here is the generalized LSX scaling with some minor modifications to allow for incorporating some newer results [8, 10]. It is based on the Lower Hybrid Drift (LHD) instability scaling initially observed in the LANL FRX experiments for the particle confinement where $\tau \sim {r_s}^2/\rho_i$ [1, 2]. As ρ_i is not a routinely measured quantity, one can employ radial pressure balance to restate it in terms of the plasma density,

$$n_0 \kappa_B T_{tot} = \frac{B_e^2}{2\mu_0} \Rightarrow n^{1/2} \sim \frac{B_e}{T_i^{1/2}} \sim \frac{1}{\rho_i} \tag{1}$$

where ρ_i is the mean ion gyroradius. One can thus restate the LHD particle confinement scaling as $\tau_N \sim n^{1/2} {r_s}^2$ It is noteworthy that the particle diffusion coefficient does not explicitly depend on the FRC scale. With the LSX data, as well as results from other experiments [10, 15], a dependence on x_s, the dimensionless ratio of the FRC separatrix radius, r_s, to the effective confining coil radius r_c, was observed. Additionally, a dependence on FRC elongation, ε, was also inferred from the data. Both dependencies would be expected as will be discussed. The empirical particle scaling coefficient consistent with both past and present experiments can be stated as:

$$\tau_N = 4.8 \times 10^{-13} \varepsilon^{1/2} x_s^{0.8} r_s^2 n^{1/2} \quad 0.35 \leqslant x_s \leqslant 0.55. \tag{2}$$

This scaling is also consistent with experiments at TAE that did not involve external manipulation of the FRC with neutral beams or plasma injection on the open field lines with electrical biasing. It is perhaps not surprising that these techniques improved the confinement as they directly affect the primary transport issue which is the steep pressure gradient at the FRC separatrix. The transition is eased by having a subpopulation of large orbit ions that can travel well beyond separatrix while still being confined inside the FRC. Injecting plasma on the open field lines near to the separatrix of the FRC (commonly referred to as the scrape off layer (SOL) in tokamak terminology) would improve the density profile there. This however comes with the significant penalty of a large energy input into an essentially unconfined plasma which can rival the energy lost from FRC in its absence.

2.1.2. FRC confinement scaling with x_s. As indicated in equation (2), the data used for x_s confinement scaling was obtained over a relatively limited range. Due to axial force balance, the average plasma pressure must be large inside the FRC over this range of x_s ($0.85 \leqslant \langle\beta\rangle \leqslant 0.94$) which results in a high plasma pressure at the separatrix. Due to unconstrained axial flow in the SOL, the result is a large radial pressure gradient. This condition is however preventable without recourse to high power neutral beams or plasma injection onto the open diverter field lines. It comprises one of the guiding principles for the successful operation of the CFR2. It is critical to have the edge density and temperature low at the FRC separatrix boundary with the open diverter flux, just as it is for the tokamak and other magnetic fusion plasma devices. Not achieving this would severely limit the ability of the FRC to meet or maintain the required fusion parameters and transport for fusion gain. The β at the separatrix can actually be kept quite low if the x_s is sufficiently large as can be readily seen in figure 3. It is clear from these two profiles that if the FRC can be maintained at high x_s, one can achieve the necessary isolation of the bulk FRC plasma from the turbulent transport conditions in the scrape-off layer.

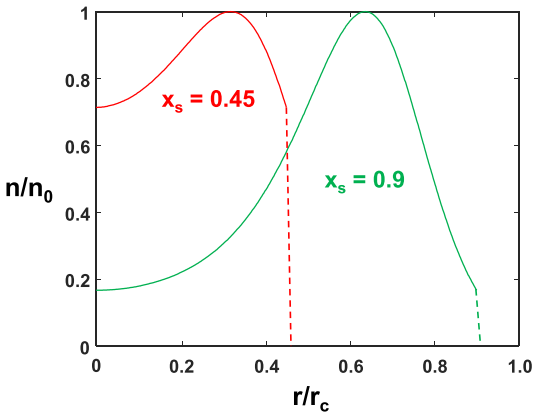

Figure 3. Ratio of the separatrix density to peak density at the FRC null as a function r normalized to the coil radius for two values of x_s. Here a RR profile was assumed for the FRC with spatially constant temperature.

High x_s FRCs were not typically achieved in past FRC experiments due to the necessity of rapidly increasing the FRC ion temperature to achieve kinetic stability to the tilt and other destructive MHD instabilities during FRC formation. This required a significant FRC compression after field reversal thus reducing the separatrix radius into the range indicated in equation (2). More pertaining to this topic will be covered later, but it is important to first understand how operation at large x_s can significantly enhance the particle confinement.

It is reasonable to assume that as the separatrix pressure decreases, the particle and energy loss rate would be proportionately reduced. For the RR profile the ratio of null to separatrix density scales as $\cosh(K_{RR})^2$ where K_{RR} is the RR profile factor which is a function of x_s. A plot of this ratio as a function of x_s is found in figure 4. Thus, operating at high x_s can achieve the necessary isolation of the bulk FRC plasma from the turbulent transport conditions in the scrape-off layer. From figure 4 transitioning from as x_s of 0.42 to 0.85—the target value of the CFR2 from formation through burn—would result an increase in confinement time by a factor of 3.7. The energy confinement would likely improve as the FRC plasma would be more magnetized between the null and edge due to

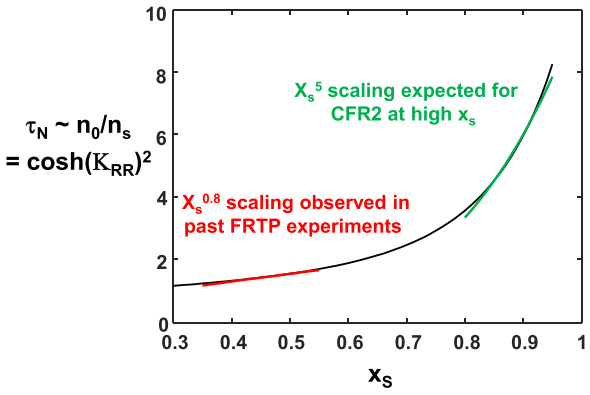

Figure 4. Ratio of the null density to separatrix density as a function of x_s assuming a RR profile.

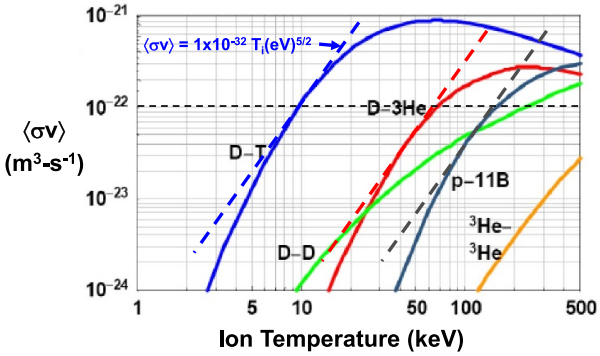

Figure 5. Fusion cross-sections for various possible fusion fuels. Dashed lines indicate a reaction rate slope that reflects an ion temperature that scales as $T^{5/2}$.

the lower average β. This would allow for a much larger temperature gradient within the FRC. Thus, along with reduced particle loss, the energy lost with each particle would also be reduced. From figure 4 the correction for the particle confinement stated in equation (2) at large x_s would be:

$$\tau_N = 1.9 \times 10^{-12} \varepsilon^{1/2} x_s^5 r_s^2 n^{1/2} \quad 0.8 \leqslant x_s \leqslant 0.95. \tag{3}$$

2.1.3. Fusion gain. The fusion reaction rate, dN_{fus}/dt, for D–T fusion systems, and in particular for the FRC is given by:

$$\frac{dN_{fus}}{dt} = \int_{vol} n_D n_T \langle\sigma v\rangle \, dVol \simeq \frac{1}{4}\langle\beta\rangle n_0^2 \langle\sigma v\rangle_{DT} Vol_{FRC} \tag{4}$$

where n_0 is the number density at the FRC null, and $\langle\sigma v\rangle_{DT}$ is the reaction rate parameter for the specified fusion reaction as a function of ion temperature T_i. It was also assumed in equation (4) that $n_D = n_T = {}^1/_2 n_i$. For pulsed systems such as the CFR2 the relevant quantity is the total fusion energy yield per pulse. Consequently, equation (4) should thus be integrated over the lifetime of the FRC plasmoid and then multiplied by the repetition rate R_p. For the purposes here it will be sufficient to multiply the left-hand side of equation (4) by the FRC energy confinement time. The energy confinement time is assumed to be 2/3 of the particle confinement time to account for any radiative, convection and conduction losses. This correction factor was basically what was observed in the LSX experiments [4, 6]. The total fusion energy provided by the D–T reaction is $E_{fus} = N_{fus}\cdot(22.4\,\text{MeV})\cdot(1.6 \times 10^{-13}\,\text{J MeV}^{-1})$. This includes an additional 4.8 MeV from the lithium fusion in the blanket necessary for generating a new triton for continued reactor operation. With this one can write for the FRC:

$$E_{fus} \cong 9 \times 10^{-13} \langle\beta\rangle n_0^2 \langle\sigma v\rangle \, Vol_{FRC} \, \tau_N. \tag{5}$$

The fusion gain scaling is derived from previous FRC particle confinement data but now demonstrating different scaling for the two regimes of x_s shown in figure 4. The fusion cross section within the range of ion temperatures from 7 keV to 14 keV as shown in figure 5, and scales as $T_i^{5/2}$. This is also the optimal range for FRC fusion in D–T as well as the target range for CFR2. Substituting for the confinement scaling as well as this fusion cross section dependence in equation (5), yields two expressions for the fusion energy yield for the two regions indicated in figure 4:

$$E_{fus} = 0.8 \times 10^{-10} (n_0 \kappa_B T_{tot})^{5/2} \varepsilon^{1/2} x_s^{0.8} r_s^2 \cdot Vol_{FRC} \tag{6a}$$

for $0.3 \leqslant x_s \leqslant 0.55$ and

$$E_{fus} = 3.0 \times 10^{-10} (n_0 \kappa_B T_{tot})^{5/2} \varepsilon^{1/2} x_s^5 r_s^2 \cdot Vol_{FRC} \tag{6b}$$

for $0.8 \leqslant x_s \leqslant 0.95$. It was assumed in equation (6) that $T_i = T_e = T_{tot}/2$, and the variables were organized to demonstrate that the fusion yield scales as the product of density and total FRC temperature raised to the power of five halves. From equation (1) the radial pressure balance between the external magnetic field pressure and plasma pressure allows for the density and ion temperature dependence to be replaced with a magnetic field dependence. The energy from fusion thus scales as B_e^5.

The expression for the FRC internal energy, again employing radial pressure balance, can be restated as:

$$E_{FRC} = \frac{3}{2} n_0 \kappa_B T_{tot} \langle\beta\rangle Vol_{FRC} = \frac{3}{4\mu_0} B_e^2 \, Vol_{FRC}. \tag{7}$$

The fusion gain, G, is defined as the ratio of the fusion energy to the FRC energy:

$$G \equiv \frac{E_{fus}}{E_{FRC}} = 1.26 \times 10^{-2} \varepsilon^{1/2} x_s^{-0.2} B_e^2 \varphi_p \; (0.3 \leqslant x_s \leqslant 0.55) \tag{8a}$$

$$G \equiv \frac{E_{fus}}{E_{FRC}} = 5.0 \times 10^{-2} \varepsilon^{1/2} x_s^4 B_e^2 \varphi_p \; (0.8 \leqslant x_s \leqslant 0.95), \tag{8b}$$

where the expression for the FRC poloidal flux φ_p is that for a RR profile, $\varphi_p = x_s r_s^2 B_e$. The fusion gain thus depends only on the product of the magnetic field squared and the poloidal flux, along with two non-dimensional variables. The gain curves for a given poloidal flux and magnetic field are shown in figure 6.

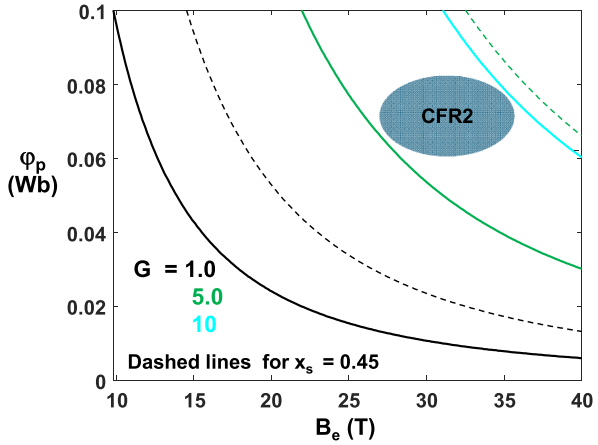

Figure 6. Gain contours as a function of the FRC poloidal flux and compression magnetic field for $x_s = 0.85$ and $\varepsilon = 15$.

It is noteworthy that there is no explicit dependence on the physical scale of the reactor, implying no inherent disadvantage for a small, compact FRC reactor. In fact, the situation is quite the opposite. For large external magnetic fields, the smaller coil experiences a significantly reduced hoop force. Given the high energy density of the FRC, a small reactor will also benefit from a more favorable reacting volume to first wall area. The expected operating region for the CFR2 is indicated on the plot in figure 6 and serves as the target values of flux and magnetic fields, details of which will be presented in section 4.

The CFR2 is designed to have a reactor inner wall diameter of 0.12 m. This small scale allows for the maximum magnetic fields and so minimizes the FRC poloidal flux required. As will be discussed in section 3, this aspect is critical as both FRC formation and stability issues incurred at high flux significantly reduce the operating window for achieving fusion gain. The LSX experiment was specifically tasked with evaluating the stability of the configuration. Despite the premature termination of these studies, it was determined that the point at which confinement scaling deviated significantly from that given in equation (2) was characterized by the equilibrium s parameter. The s parameter is defined as:

$$s \equiv \frac{1}{r_s}\int_R^{r_s} \frac{r}{\rho_i}\,\mathrm{d}r \cong 1.52\frac{\varphi_p\,(\mathrm{mWb})}{r_s\,(m)\,\sqrt{A_i T_i\,(\mathrm{eV})}}, \qquad (9)$$

where the expression on the right is stated in terms of the experimental variables for the FRC. Here A_i is the atomic mass of the ion. The s parameter is roughly a measure of the average number of ion gyro-orbit radii between the null radius, R, and the separatrix radius, r_s. It was found that for values of greater than about 4, confinement plateaued and then rapidly decreased [6].

2.1.4. FRC fusion with advanced fuels. For FRC concepts employing advanced fuel cycles, figure 6 indicates the extreme difficulty for these fusion cycles due to the significantly lower reaction rates for the same plasma pressure (or $B_e{}^2$ for the FRC). Achieving fusion gain with the FRC, or any other fusion scheme for that matter, is far easier with D–T as figure 5 attests.

The preference for the D-^{3}He fusion reaction stems from its aneutronic nature producing only a proton and an alpha without the need to manage high energy neutrons as it is with the D–T reaction. The side D–D reaction with its neutron byproduct however considerably undermines the notion that operation of a D-^{3}He reactor would be aneutronic. To mitigate this adverse side effect, as well as increase the fusion yield, a substantially higher operating temperature than D–T is required. From figure 5 an increase in ion temperature of a factor of seven is necessary to achieve the same reaction cross-section as D–T, as well as minimize the D–D reaction rate.

Despite these drawbacks, FRC based D-^{3}He reactor scenarios have been investigated for many years [16]. The interest is primarily due to the high beta nature of the FRC which significantly curtails the synchrotron radiation losses encountered in magnetized plasmas at higher electron temperatures, as well as a much less deleterious neutron environment. However, a more critical issue than the higher temperature, is the extreme rarity of the Helion (^{3}He) isotope as it constitutes only 0.000 137% of Helium on Earth. Unlike Tritium, Helion is a stable isotope as well as the decay product of Tritium which is the main source of Helion available today. With the demonstration of the supersonic FRC compression and merging technique at MSNW [7], a methodology was also developed to generate an appropriate environment for D-^{3}He reactor, as well as for the direct conversion of the high energy proton into electricity. This development lead MSNW to spinoff a company, Helion Energy, to pursue this goal. To provide the necessary ^{3}He, it was shown [17] that the reactor could be operated with a Tritium-depleted, self-sustained, catalyzed D–D fuel cycle where both the tritium and ^{3}He produced would be recovered on each pulse. The tritium would be allowed to decay allowing for both fusion products to be reused. In this manner it would be possible to sustain the D-^{3}He fuel cycle with as much as 16% of the fuel being ^{3}He with no need for an external source of Helion.

It is worth examining what the fusion gain from the cross-section data for D-^{3}He under the same relevant FRC conditions (i.e. x_s, ε, B_e and φ_p). The fusion gain for this fuel cycle compared to D–T cycle given by equation (8*b*) is greatly reduced for the same reactor parameters. Firstly, in order to compensate for the sevenfold increase in temperature to achieve the same reaction rate, radial pressure balance with the same external magnetic field requires that the plasma density to decrease by a factor of seven. Furthermore, according to (3) the FRC confinement time, τ_N, which scales as $n^{1/2}$ must also decrease. Finally, the fusion energy dependence on FRC parameters stated in equation (5) which was derived from equation (4) included a factor of ¼ reflecting the fact that n_D and n_T are both half of the total ion density, which is the optimal value. For the self-sustained D-^{3}He fuel cycle discussed above, it was determined that the fractional concentration of ^{3}He was limited to roughly 0.16 [17]. The product of n_D and n_{He3} is therefore (0.16)·(0.84) = 0.1344, which is a factor

0.534 times smaller than the balanced D–T. From equation (5) the total reduction in fusion energy gain for D-^{3}He from D–T is therefore $(1/7)^{2.5}\cdot(0.134/0.25) = 0.004$. Whatever possible reactor benefit there could be for employing a partially aneutronic fusion reaction it is highly doubtful that it would make up for the D–T gain advantage of 240. As will be detailed in sections 4.3 and 5.2, aneutronic fusion has other problems related to the fusion energy being retained in the plasma rather than escaping into the blanket. These issues pertain to both energy conversion efficiency and rapid gain reduction during fusion burn.

From figure 5 and the preceding analysis, it is evident that the P-^{11}B fuel cycle would only be that much more challenging, with a reduction in gain by factor of 800 or more from operation in D–T. Although obtaining the nuclear fuel would be vastly easier, and the neutron generation orders of magnitude lower, the fusion gain, even with classical confinement, is near unity. The high temperatures required severely complicate the FRC generation, and energy conversion technology becomes difficult in the extreme due to the intense radiation from the electrons and particle-wall interactions from the plasma and fusion product alphas.

3. Compact FRC fusion reactor key physics

3.1. FRC poloidal flux retention and loss mechanisms

3.1.1. Poloidal flux loss during formation. The ultimate goal of the CFR2 concept is to achieve the target region of poloidal flux and confining magnetic field as indicated in figure 6 necessary for D–T fusion gain. The challenge is to accomplish this starting with a cold partially ionized gas in a sub-Tesla magnetic field. The FRTP formation technique will be used as it is the only method proven effective in creating the well-confined FRC plasmas. This process is a challenging one as the FRC begins as a closed magnetic configuration that is not in equilibrium [$P \neq P(\psi)$]. Plasma must flow from the initial reversed magnetic field onto the external magnetic field as it enters radially through the dielectric vacuum wall into the vacuum chamber as the magnetic field is reversed.

Upon 'lift-off', which is the point in time during field reversal when the separatrix of the FRC passes through the vacuum boundary and the inward pressure of the rising external magnetic field compresses the FRC away from the vacuum wall, several additional challenges emerge. At this juncture, the FRC is prone to instability from both interchange ($N > 1$—fluting) and co-interchange ($N = 1$, $M = 1$—tilting) modes. Poloidal flux is rapidly lost until sufficient flux has been annihilated by turbulent flow that leads to ion heating and kinetic stability [18]. At moderate to large s values on LSX ($3 < s < 5$) flutelike separatrix distortions are observed in the end-on filtered (510–600 nm) as well as soft x-ray plasma images during the formation phase of the higher s FRC's on LSX (see figure 7). The fluting distortions seen during the radial formation stage are Rayleigh–Taylor instabilities driven by radial and axial accelerations, rather than intrinsic FRC tilt stability. These distortions occur when the plasma ions are cold, and the FRC is still at large radius and has retained

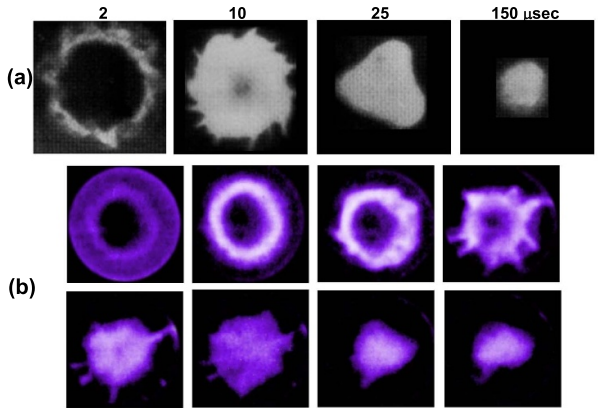

Figure 7. End-on images during formation at moderate s. (a) Soft x-ray images taken on *in situ* formation on LSX taken at times indicated. (b) End-on filtered (510–600 nm) images taken employing Dynamic Formation (xx) on the pulsed high-density experiment (PHD) at the University of Washington (UW) Here the first image was taken at 5 μs and at intervals of 5 μs.

most of its lift-off flux. From equation (9) it is evident that at this time the FRC has a very high effective s value. Higher mode numbers were also seen during the peak axial compression phase of formation with the dominant mode number, N, cascading downward to lower N in time, so that typically by the equilibrium phase no significant distortions of the separatrix were observed. The emergence of interchange modes during formation at higher s values aligns with expectations from finite Larmor radius (FLR) theory [19]. The condition derived for stability in a cylindrical configuration [20] can be approximately expressed as:

$$\frac{\rho_i}{r_s} > \frac{N^{1/2}}{N-1}\frac{r_s}{L_s} \tag{10}$$

where it was assumed that the average radius of curvature $\sim {L_s}^2/r_s$. For a FRC where $s \sim 0.5(r_s/\rho_i)$, flute instabilities may occur for mode numbers where

$$\frac{N-1}{N^{1/2}} < \frac{s}{\varepsilon}. \tag{11}$$

For a typical transient elongation of 3 and a formation s value of 6, one would expect flutelike modes with N up to 5, which aligns with observations. As the FRC elongation typically increases as it FRC relaxes into equilibrium, the fluting is observed only transiently during *in situ* formation.

Extensive experimental studies on the parameters and dependencies of FRCs during formation were carried out [21–24] from which the following conclusions for attaining the high poloidal flux desired here.

(1) Lift-off flux is maximized by utilizing a multipole barrier field at the vacuum boundary during field reversal. However, the magnitude of the field penetration must be limited as the presence of this field inhibits the electrons from carrying the induced currents thereby forcing the ions to carry it. This induces premature rotational instability characteristic of the termination phase of the FRC.

(2) The maximum lift-off flux normalized to the chamber cross-sectional area is limited to roughly 0.1 T. This limitation arises due to increased flux loss at larger bias fields during field reversal as both the reverse field gradient and timescale for reversal increases. Consequently, substantial wall heating occurs leading to vaporization and ablation. Barrier fields mitigate this effect though impurity concentration still correlates with increased bias flux.
(3) The D_2 fill pressure for maximum lift-off flux scales inversely with radius allowing larger vacuum chambers to operate optimally at a lower fill pressure and thus achieving higher ion temperatures and greater stability. This scales roughly with the vacuum inner wall radius. For instance, the optimal fill pressure for the TRX device ($r_w = 10$ cm) was 15–20 mTorr whereas for LSX ($r_w = 40$ cm) it was 4–5 mTorr.
(4) Poloidal flux retention is dependent on formation timescale which is set by the initial E_θ applied at the vacuum wall. Optimal E_θ is $\sim$ 20–25 kV m^{-1}. However, LSX was closer to 10 kV m^{-1}. Resistive 2D MHD calculations indicate that this suboptimal E_θ reduced the equilibrium FRC poloidal flux by at least a factor of 2 to a maximum of $\sim$10 mWb.
(5) Final flux retention into the FRC equilibrium phase was 1/3–1/2 the lift-off flux for moderate to low s FRCs exhibiting optimal lifetimes.

Guided by these results, one can now determine the general scale, as well as plasma and circuit parameters that will yield the equilibrium poloidal flux for a fusion gain of 5 or more in D–T. As indicated in figure 6 for the CFR2, the reactor poloidal flux desired is approximately 75 mWb, presuming a high magnetic field ($\sim$30 T) can also be achieved. If no more than 25 mWb of flux is lost from formation to eventual high field burn, the lift-off flux must be at least twice the 100 mWb or 0.2 Wb. For this to be at a bias magnetic field no greater than of 0.1 T normalized to the vacuum wall area, a wall radius of 0.8 m is required which is double that of LSX. For optimal flux retention, an $E_\theta \sim 20$ kV m^{-1} at the wall would necessitate a loop voltage of 100 kV. The coil voltage will be higher still as this must be positioned outside the dielectric vacuum chamber wall. With a reasonable value for the wall thickness, coil radius of 0.84 m would be feasible implying a coil voltage of 110 kV. This is likely doable with a multi-segmented formation coil employing stacked high voltage solid state switches for repetitive pulsing.

To achieve maximum fusion gain, but to also avoid significant losses in attaining the high compression ratio required, it is essential to reach both a high ion temperature and high x_s from the outset. At the desired x_s of 0.85 with an effective coil radius of 0.85 m and an FRC poloidal flux of 0.1 Wb the external magnetic field would be a modest 0.22 T which is quite far from the reactor values of 30–35 T. This indicates that substantial compression of the FRC is necessary. The following sections will address how to accomplish this in a manner that takes into account the stability and good confinement operational space available to the FRC and have the FRC be located in that space throughout the entire compression phase.

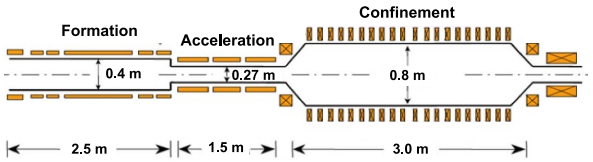

Figure 8. Experimental layout of the coil set at the University of Washington Redmond Plasma Physics Laboratory.

This objective is precisely what the staged compression of the FRC was designed to achieve.

3.2. Formation and acceleration of the FRC

Once the FRTP method was found capable of creating long lived FRCs, experiments were carried out and successfully demonstrated the ability to translate the equilibrium FRC to another chamber [25]. Further investigation in experiments at Osaka University [26, 27] it was found that the FRC once formed could be translated into a large, low field chamber at supersonic velocities. The ion directed energy was then rethermalized after interacting non-adiabatically upon reflection with the downstream magnetic mirror field. The FRC translation was advanced further in experiments at the UW where an FRC was formed and translated into a smaller chamber where several coils that were energized in a peristaltic manner to further increase the FRC velocity and thus kinetic energy. A schematic of the experimental setup can be found in figure 8. The excluded flux radius profiles for a typical discharge are shown in figure 9 at various times during the process. From the first pass of the FRC in the confinement chamber, assuming a RR profile, the poloidal flux is estimated to be 3 mWb with a stable s/ε value of 0.4. The FRC reaches a maximum velocity of 300 km s^{-1}. After reflecting off the downstream mirror field the FRC temperature increased to near 400 eV (see figure 10) with almost all the kinetic energy going to increased temperature in the ions. One can gain insight as to the nature of the plasma disequilibrium during the powerful interaction with the downstream mirror from the 2D resistive MHD calculation which is shown in figure 11. Such a strong and rapid reversal assures the non-isentropic behavior of the interaction thereby promoting thermal conversion. Remarkably, the FRC does not exhibit significant plasma or flux loss from this event. It is worth noting from figure 10, on the first pass ($\sim$30–35 μs) the FRC flux based on the RR profile is 3 mWb, which is consistent with the 2D resistive MHD model with LHD equilibrium scaling. On reflection and the subsequent FRC expansion due to thermal conversion, the inferred RR flux would be an increase to 11.4 mWb. This unexplained flux amplification would put the FRC into the regime of tilt instability ($s/\varepsilon > 1$). Given the discussion of the effect of mirror confinement and the results of figure 2, a more reasonable explanation is that the FRC is mirror confined which is also supported by the experimental results of figure 9.

These results are notable for two reasons: firstly, the FRC, once it has reached a quiescent and stable equilibrium, exhibits a robustness that tolerate both acceleration to supersonic

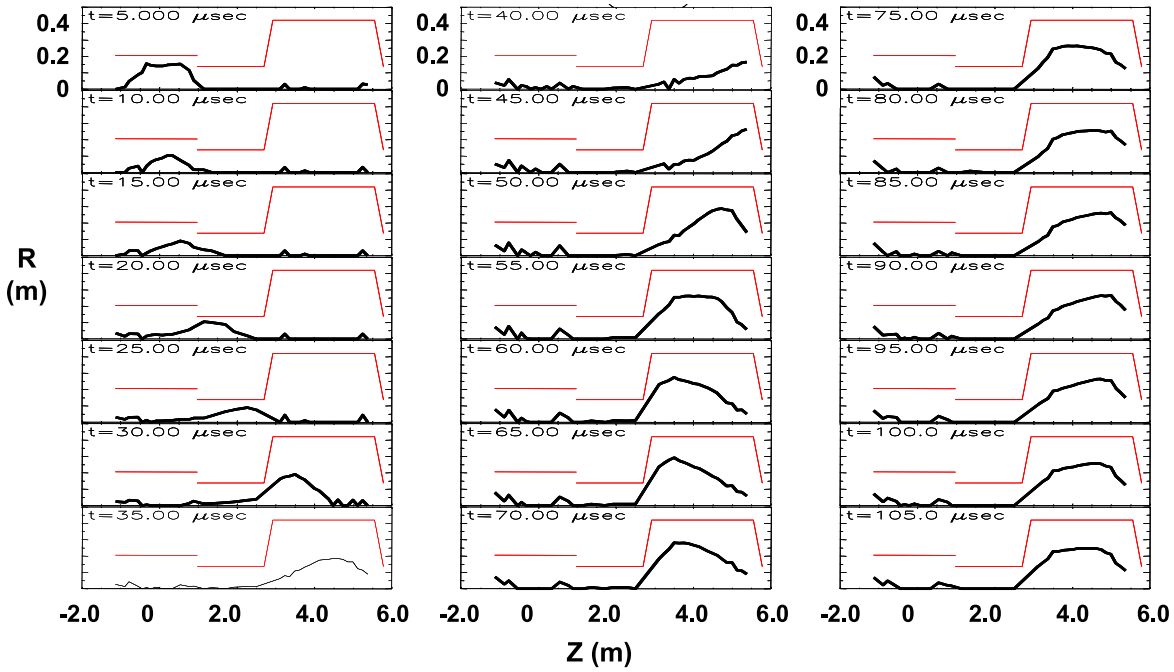

Figure 9. Experimental measurements of excluded flux radius, $r_{\Delta\varphi}$ obtained from external B and flux loop arrays. For the central regions of the FRC, $r_{\Delta\varphi} \cong r_s$. Frames start at 5 μs after initiation of field reversal and are displayed thereafter at 5 μs intervals.

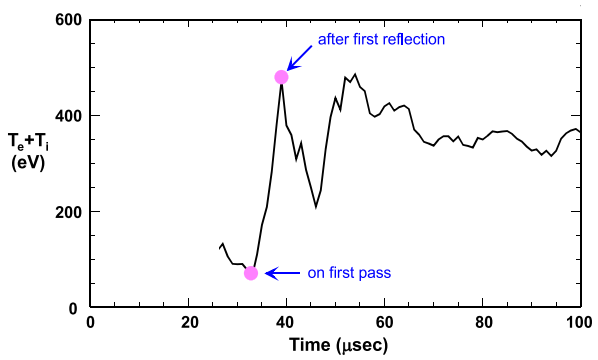

Figure 10. FRC temperature determined by pressure balance with external axial magnetic field as a function of time.

velocities as well as rapid deceleration without significant loss of particles or flux. Secondly, expanding the FRC into a larger chamber does not make much headway toward closing the gap of making the FRC into a fusion plasma as the increased temperature does not compensate for the reduction in density.

3.2.1. Dynamic formation of the FRC. The dynamic formation of the FRC was initially demonstrated at MSNW as part of research on a plasma thruster for space propulsion [28]. It was then incorporated into the Inductive Plasma Accelerator FRC experiments for fusion [7, 29]. It has since been employed at other facilities [30, 31]. This novel formation technique has been shown to appreciably enhance the FRC magnetic flux and initiate rapid translation. The lower plot in figure 12 illustrates the dynamic formation (DF) procedure with 2D MHD calculations based on experiments carried out on the Pulsed High Density (PHD) device at the University of Washington (UW) [32, 33]. Dynamic formation ensures that the resultant FRC is established on the fastest possible timescale minimizing the time the FRC is out of equilibrium when both flux and particles are rapidly lost. Figure 12 demonstrates that with the sequential reversal of the axial array of small aspect ratio formation coils, the FRC flux is maintained until the last coil is reversed. By this time much of the FRC has been substantially formed and accelerated to high velocity. With an aggressive sequential coil timing interval, the FRC kinetic energy can actually exceed the thermal energy.

DF, however, can be problematic when attempting to achieve supersonic velocities while simultaneously compressing the FRC. This issue becomes increasingly significant as the formation coil and chamber radius increase. Experimental data from the PHD experiment highlight the complexities involved with applying DF in conjunction with FRC compression. As depicted in figure 7, the FRC stability parameter s/ε resides persistently within the unstable regime post lift-off. DF intensifies the density gradients that drive instability. The objective of maintaining the FRC in a low flux-loss configuration throughout its formation and compression is thus impeded from the outset. The increase in ion temperature required to achieve stability against co- and interchange instabilities occurs too late in the process.

A picture of the experimental layout of the PHD experiment can be found in figure 13. The dimensions and operation can be gleaned from the lower plots from 2D MHD calculations shown in figure 12. Three distinct modes of formation were

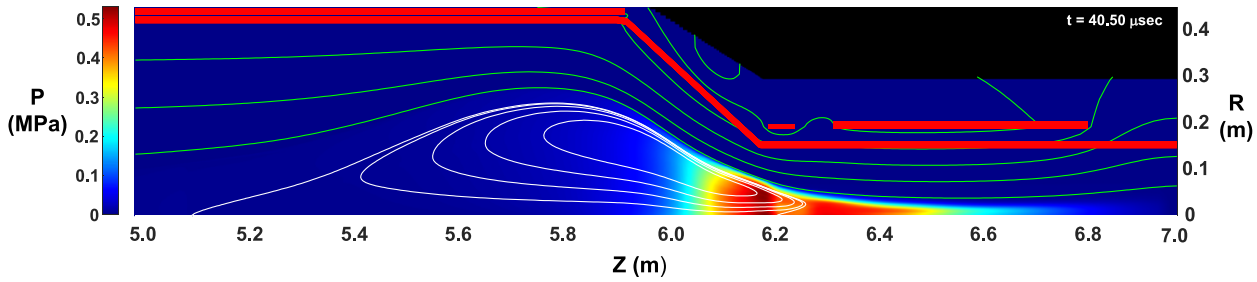

Figure 11. Results from a 2D resistive MHD calculation for data shown in figure 10. Plotted are the magnetic field lines and pressure contours at the turn around point in time when the FRC average axial velocity has reached zero. White lines correspond to closed FRC poloidal flux and green lines to the flux from the external coils.

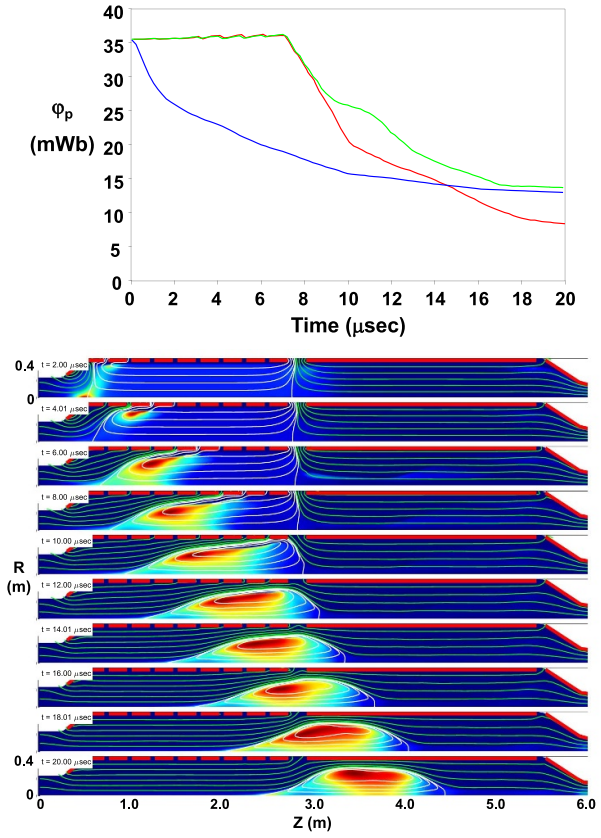

Figure 12. (Top graph) Flux loss from the 2D resistive MHD calculation for (1) dynamic formation (DF) of the FRC followed by flux compression (red trace), DF followed by translation into a similar radius chamber (green trace) and standard *in situ* formation (blue trace). (Bottom) Time sequence at 2 μs intervals for the FRC formation and translation case.

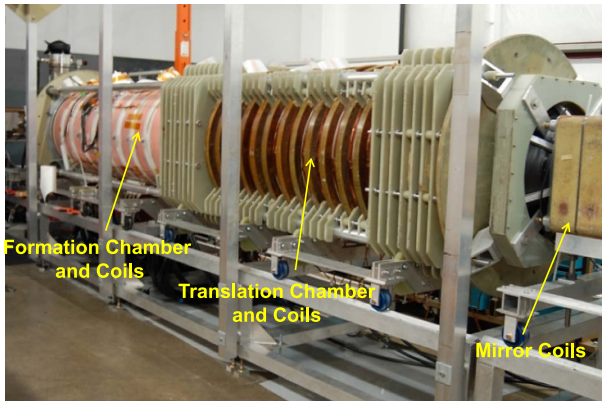

Figure 13. The PHD experiment at the UW Plasma Dynamics Laboratory.

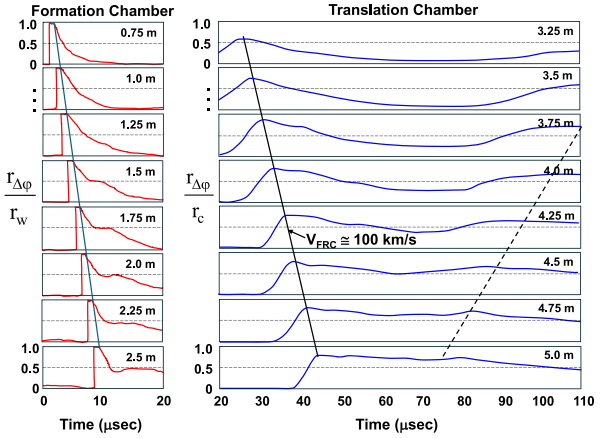

Figure 14. Plots of FRC excluded flux radius normalized to coil radius verses time at various axial locations in source (left) and translation chamber (right). The external magnetic field instrumentation does not extend into the end cones.

studied; (1) DF followed by compression (2) DF for translation into a containment chamber, and (3) Standard *in situ* formation where all coils are energized simultaneously.

The temporal sequence from the resistive 2D code shown in figure 12 corresponds to the DF for translation case (green trace in the upper figure) which align with the experimental results on PHD which can be found in figure 14. Unlike mode (1), in this case the energy storage for the formation coils was reduced to minimize compression of the FRC after formation. This approach assured the FRC could remain at high x_s throughout formation as well as translation.

As indicated in figure 14 the FRC velocity was significantly reduced to a subsonic value, and little decay in the flux was observed in the transport chamber. The velocity after reflection did not reflect a purely isentropic one, but it was sufficient to send the FRC back into the source where it terminated on

the upstream wall. Unfortunately, all research funding related to FRCs was suspended before this mode of FRC operation could be fully studied. The fact that the FRC can be formed and translated at moderate, subsonic speed at high x_s is crucial to the CFR2 concept which will be discussed further in section 4.

The resistivity temporal profile assumed in the code calculations in figure 12 divides into two time periods. Initially, the resistivity profile is anomalous where the anomaly extends from the FRC separatrix all the way inward to the null. A temporally constant numerical coefficient was identified that replicated the observed flux losses observed on LSX during formation across the entire range of data collected and is based on the s/ε parameter. This '*s*' resistivity is applied from the initiation of FRC formation as virtually all FRCs start with an s/ε value that exceeds unity. It has also been observed experimentally that due to the turbulent nature of this flux loss, the ions are predominately heated, causing the s/ε value to eventually fall below unity from a combination of both ion heating and flux loss. At this juncture the code resistivity transitions to that characterizes LHD transport observed in the FRC equilibrium phase.

The persistently high resistivity at the null where the gradients in magnetic field and pressure are low warrants an explanation. It is hypothesized that the anomalous flux loss has to do with the FRC's asymmetric dynamical behavior that characterizes both the FRC formation and to a lesser extent the equilibrium at high s/ε. Certainly, the images of figure 7 give support to this interpretation. A likely mechanism that cannot be modeled in the 2D code is the tilting motion of the FRC. The impact of this motion on the closed poloidal flux will now be described.

3.2.2. FRC flux loss from formation instabilities. It is important to understand the consequences of the formation methodology, scale and initial conditions necessary to reach fusion conditions. Several factors were considered and enumerated in section 3.1.1 such as the optimum scale and fill pressure for minimizing formation flux loss. Issues with dynamic formation of the FRC at large scale as well as high flux have been indicated in the prior section. Even for *in situ* formation, as in LSX, there appears to be a minimal yet unavoidable loss. The primary factor that would explain virtually all the data from prior experiments is the initial lack of kinetic stabilization (i.e. $s/\varepsilon > 1$) of the MHD instabilities that affect the FRC at this time. Initially, it is primarily the internal profile asymmetry, but this resolves in typically less than an ion axial transit time. The development of both the interchange (fluting) and co-interchange (tilting) modes, however, continues. Rayleigh–Taylor instabilities are driven by both strong axial and radial magnetic forces, and the Kelvin–Helmholtz instability from sheared flow as the FRC is accelerated to high velocity.

The primary issue appears to be the propensity of the high s/ε FRC to deform and tilt. These motions will cause field lines at the separatrix to open and reconnect to the external magnetic field thus effectively losing flux along with plasma. As this flux-loss occurs due to a fully 3D motion, it will not be

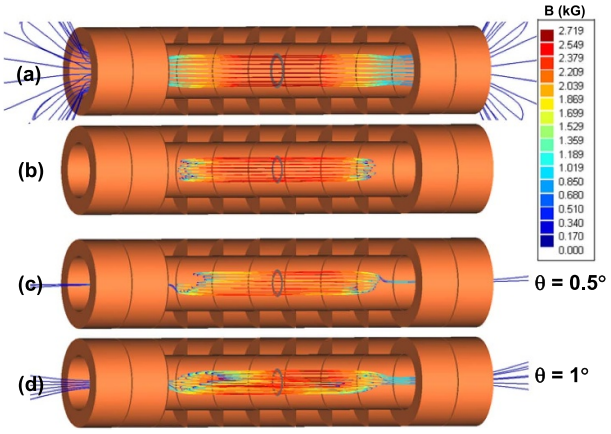

Figure 15. Cutaway showing magnetic field lines inside flux conserving coils emanating from the annulus in the midplane with magnetic field strength variation along field lines. (*a*) Field lines adjacent but radially external to the FRC. (*b*) Field lines adjacent to the separatrix but inside the FRC. (*c*) Field lines as in (*b*) but with the FRC tilted 0.5°, and (*d*) the FRC tilted 1°.

observed in the 2D calculations and can only be represented as an anomalous loss extending to the null in the code, i.e. the *s* resistivity. Azimuthal asymmetries were certainly present as indicated in the end-on imaging (figure 7) and external arrays of magnetic pickup loops [34, 35]. The effects of tilting were examined by performing 3D magnetic field calculations shown in figure 15. In case (*a*) of this figure the field lines emanating from an annulus radially outside the FRC separatrix illustrate how the field in the scrape-off layer flows to the ends of the confinement coils as expected. For case (*b*) the field lines emanating from an annulus inside the separatrix show the closed nature of the FRC fields for the axisymmetric FRC. For cases (*c*) and (*d*) it is observed that even minor tilting of the FRC leads to the opening of the field lines near the separatrix.

The procedure then for accurately modeling the behavior and confinement of FRCs across a wide range of formation methodologies configurations, magnetic fields, and timings is to apply the '*s* resistivity' until the s/ε parameter that characterizes the FRC drops below unity. At this juncture the resistivity is switched to the LHD resistivity scaling that reflects the observed particle and flux loss in equilibrium where the coefficient was empirically determined to yield the confinement times implied by LSX scaling.

However, it was found that for DF and more aggressive acceleration and compression schemes, the flux and particle loss in equilibrium would often be influenced more by numerical losses. This is due to the rapidly moving grid as the 2D code employs an adaptive Lagrangian mesh [36, 37]. This computational approach ensures a reasonable runtime while still accurately reproducing FRC dynamics, if not the decay rates for long-lived FRC equilibria.

3.2.3. Supersonic merging and compression of FRCs. From equation (8) the fusion gain scales as $B_e{}^2$ or equivalently, the FRC plasma pressure so that both the FRC temperature and density must be significantly increased after formation. A

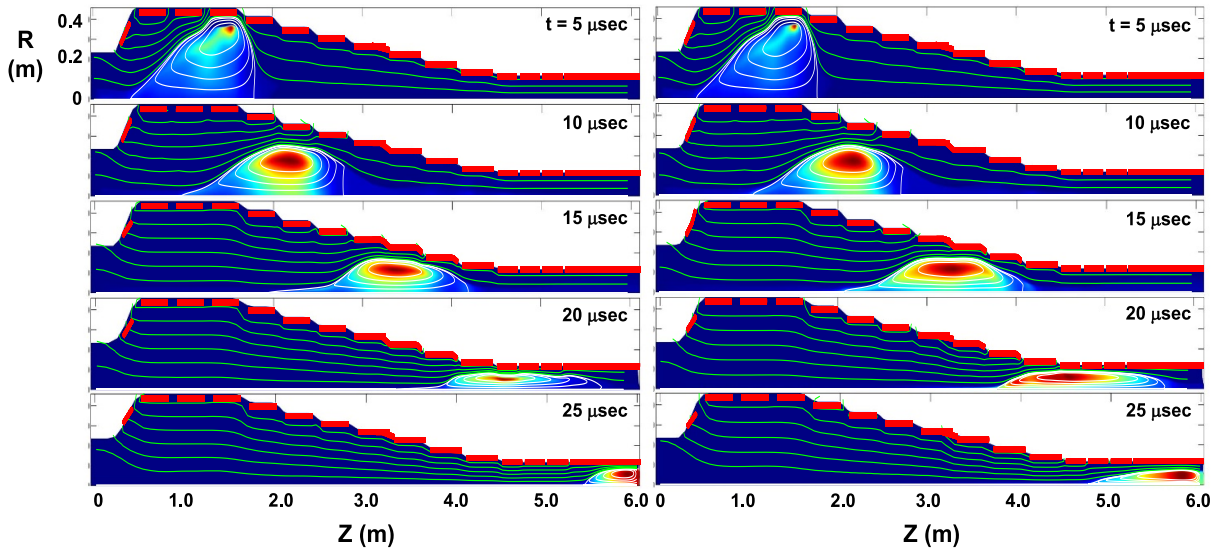

Figure 16. 2D resistive MHD calculations for the Fusion Engine design. On the left is a calculation where the resistivity is based on LHD transport but applied throughout the FRC. At right is the same starting parameters but employing an empirical resistivity based when on $s/\varepsilon > 1$, otherwise the LHD resistivity.

potential approach was devised at MSNW and referred to as the Fusion Engine [7]. It was experimentally tested at MSNW and then on a larger scale at Helion Energy [38]. The Fusion Engine concept employs two oppositely directed FRCs that are simultaneously accelerated and compressed to supersonic velocities and then merged in a central section where the kinetic energy of the FRCs is converted into thermal energy. At this point the merged FRC is further compressed to achieve fusion temperatures. This method employs DF as well as a form of axial compression to drive the FRC through a series of smaller radius coils where it continues to be accelerated and wall compressed. Figure 16 shows the 2D MHD calculation for the entire process up to merging for one of the two FRCs. Considering what has been said, this process should drive instabilities throughout the entire formation and compression. The use of a multipole barrier field would help control the large-scale distortions observed on LSX and PHD, but it was not clear what, if any, effect it would have on flux loss. In the design of the Fusion Engine, it was assumed that the flux and particle loss would not exceed that predictions based on LHD transport. These results are shown on the left-hand side of figure 16.

From the numerical simulations presented [38] the flux loss appears to be severe with only a small fraction of the flux (∼5 mWb) surviving into equilibrium. Reanalysis of the 2D MHD calculations from the original numerical calculation for the Fusion Engine but now using the s resistivity for times that s/ε is greater than unity before switching to the LHD resistivity, the results matched the flux-loss inferred from the numerical results in [38]. The code results are shown on the right side of figure 16. The corresponding time history of the FRC flux for the two cases can be found in figure 17.

Even though it appears that the FRC on the left side in the 2D calculation of figure 16 to be in an equilibrium where

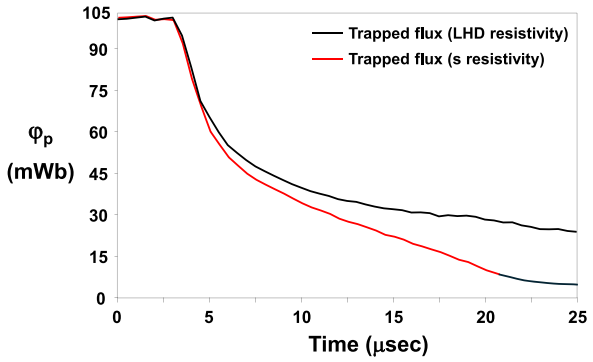

Figure 17. Plots of the flux decay for the two calculations shown in figure 17 for the Fusion Engine.

$P = P(\Psi)$, it is not likely to be in a quiescent state in 3D. To simultaneously compress and accelerate the FRC to supersonic velocity, the axial compression of the FRC needs to be aggressive and sustained throughout by maintaining a strong magnetic gradient across the FRC. The FRC does not relax into a true equilibrium until ejection into the compression chamber. The s/ε stability parameter does not fall below one until roughly this time when the FRC expands axially with the ions rapidly heated by compression. Both the relatively low ion temperature and short elongation from axial compression account for the prolonged high s/ε value and the consequent elevated flux loss rate. When axially compressed as the FRC is here, it is essentially mirror-confined. The rapid loss of flux is thus not immediately apparent from external measurements. As discussed earlier in section 2.1, the mirror confined FRCs appear to have a greater amount of flux than what is actually the case. The result is that there is little difference in FRC dimensions and behavior observed between the two cases although the difference in flux loss is pronounced

and is eventually manifested as the FRC is finally brought into equilibrium.

4. CFR2 concept

It should be noted that the approach to a CFR2 that was taken with the Fusion Engine concept illustrated in figure 16 was not without merit. The primary issue was the attempt to achieve a CFR2 with compact FRC formation while simultaneously compressing it. The idea of effectively creating a wall compression of the FRC is basically a sound concept as will be seen, but it must be executed in a manner that maintains the FRC in a stable equilibrium from the outset. Initiating with a relatively moderate FRC ion temperature was necessary in order to reach supersonic speeds at a velocity of roughly 300 km s^{-1} that could reasonably be achieved while still compressing the FRC. This along with the high flux needed for FRC fusion gain made for a very large initial s. The strong simultaneous axial and radial compression required reduced the FRC elongation leading to an s/ε greater than one for virtually the entire compression/acceleration time as indicated in figure 17.

The approach taken with the CFR2 concept is to avoid these shortcomings by adhering to the guidelines set out in section 3.1.1 and ensuring that the FRC remains in a stable state throughout. Additionally, provide the means to retain FRC in an optimal configuration for minimal transport throughout the compression process. The essential elements then are the following: (1) Form the FRC at a scale to obtain sufficient confining poloidal flux to achieve D–T fusion gain of at least five based on the modified LSX scaling for large x_s given in equation (6). (2) Ensure the scale is adequate so that the normalized liftoff flux is consistent with the empirical limit of 0.1 T, and yields the required FRC equilibrium flux. This must also be achieved at a sufficiently low fill pressure to rapidly produce an ion temperature sufficient to stabilize the FRC without the need for continued flux compression. This can be accomplished with a formation coil set where $r_c \geqslant 0.8$ m, and a length $\geqslant 4$ m at a fill pressure of 1 mTorr. (3) Form the equilibrium FRC employing a relatively weak form of DF with only enough compression and axial acceleration to produce FRC translation at subsonic velocities (100–150 km s^{-1}) at large x_s (0.75–0.85) to minimize instability and flux loss. (4) Stage the compression of the FRC employing a series of cylindrical coils of decreasing radial size that are stepped in a manner so that only small, isentropic radial compressions are needed thereby maintaining the axial velocity and equilibrium properties of the FRC. A coil radial step size reduction known to be consistent with good transport is employed for each stage ($r_c{}^{i+1}/r_c{}^{i} = 0.75$) [7].

The CFR2 device layout illustrated in figure 18 incorporates all of these considerations. The coil length was adjusted for each stage to ensure that the FRC was compressed during that stage by only radial forces, as in stationary FRC compression, but only enough to provide for insertion into the next coil stage. In this manner the x_s is maintained between 0.75 and 0.85, assuring low transport losses while realizing a wall compression of the FRC. Ten stages were necessary for the FRC to reach the desired state for the fusion burn with an x_s of 0.85, length of 1.4 m and a confining field of approximately 35 T. Detailed rationale for the design elements will now be presented.

4.1. FRC formation and compression in CFR2

As mentioned, the formation takes advantage of source size and dynamic formation to form a high temperature FRC and translate into the first compression coil at low velocity and large x_s. This much like what was done on the final PHD configuration discussed previously and depicted in figures 14 and 15. However, in this case the FRC undergoes a slight compression during the translation through the coil to facilitate entry into the next coil. This process is repeated from one coil to the next with decreasing coil radii but increasingly stronger magnetic fields as roughly the same vacuum flux fills each coil as this is essentially a wall compression.

The resistive 2D code was used to better understand the behavior of the FRC and optimize the process. Due to the large change in radial scale, as well as length of the simulation region, it was necessary to divide the calculations into two or three separate calculations reflecting roughly half of the staged compression with a restart of the calculation using the FRC parameters at the end of the previous calculation. Figures 19 and 20 show the results from the first five of the ten stages. In figure 19, the FRC maintains an equilibrium where the pressure contours align with flux surfaces. Only a single monolithic coil per stage is used for radial compression. This still allows for the FRC to coast at a relatively constant speed as it passes into progressively smaller coils. In this way the process becomes essentially an isentropic and adiabatic wall compression.

The movement of the FRC from coil to coil may require adjustments due to potential drag mechanisms. If was found in the MHD calculations that small modifications in the timing of coil initiation and changes in field risetime were observed to significantly modify the FRC acceleration and deceleration needed to keep the FRC motion constant as it transitions from coil to coil. As a result, it should be possible to experimentally adjust these parameters as well to obtain the nearly constant FRC desired.

The benefit of wall compression is that the large x_s achieved initially at large radius can be maintained all the way through to the burn chamber. From equation (3), the plasma confinement time anticipated for the FRC is over 7 ms implying a poloidal flux confinement of about 5 ms as it is typically somewhat less than the particle confinement. As can be seen in figure 20, the code calculation has a ‘code’ resistivity that is much higher. This is due to the large-scale spatial changes that the FRC undergoes in the calculation which necessitating substantial rezoning and movement of the adaptive grid. Decreasing the LHD coefficient by a factor of 10 made no change in the loss rate thus corroborating the code-based cause of the high resistivity. *In-situ* calculations demonstrate

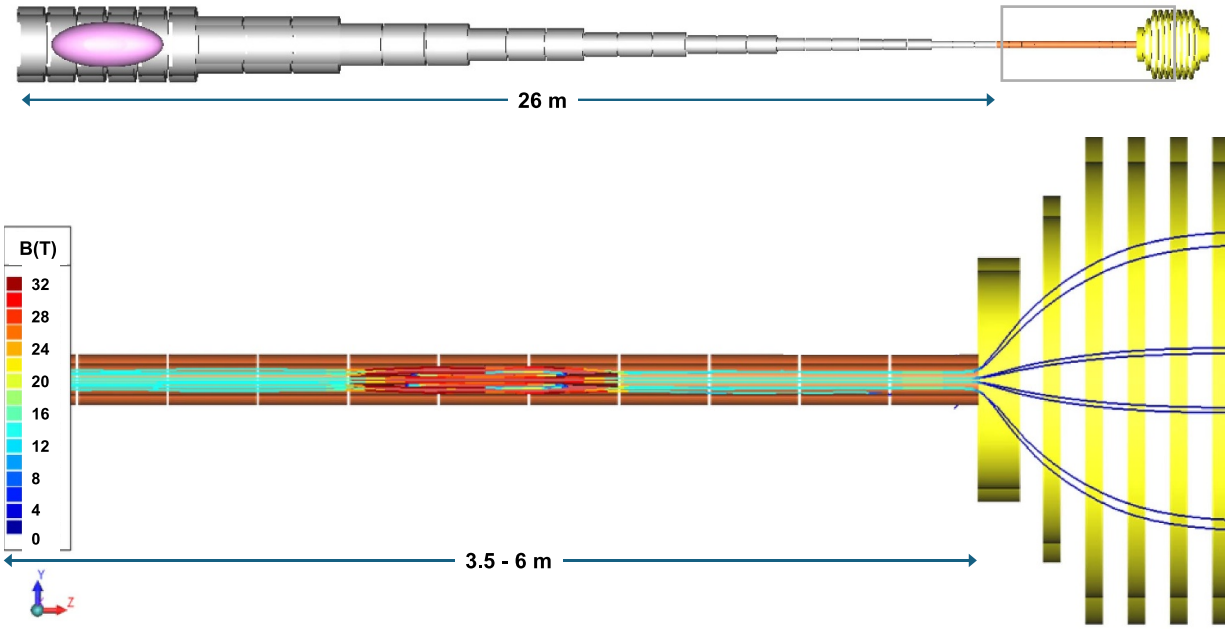

Figure 18. Top: the layout at scale of the CFR2 dynamic formation, staged compression, burn and divertor/energy recovery chamber. Bottom: expanded cross sectional view with a plot of the FRC and external field lines in the CFR2 burn chamber and divertor/energy recovery chamber coils.

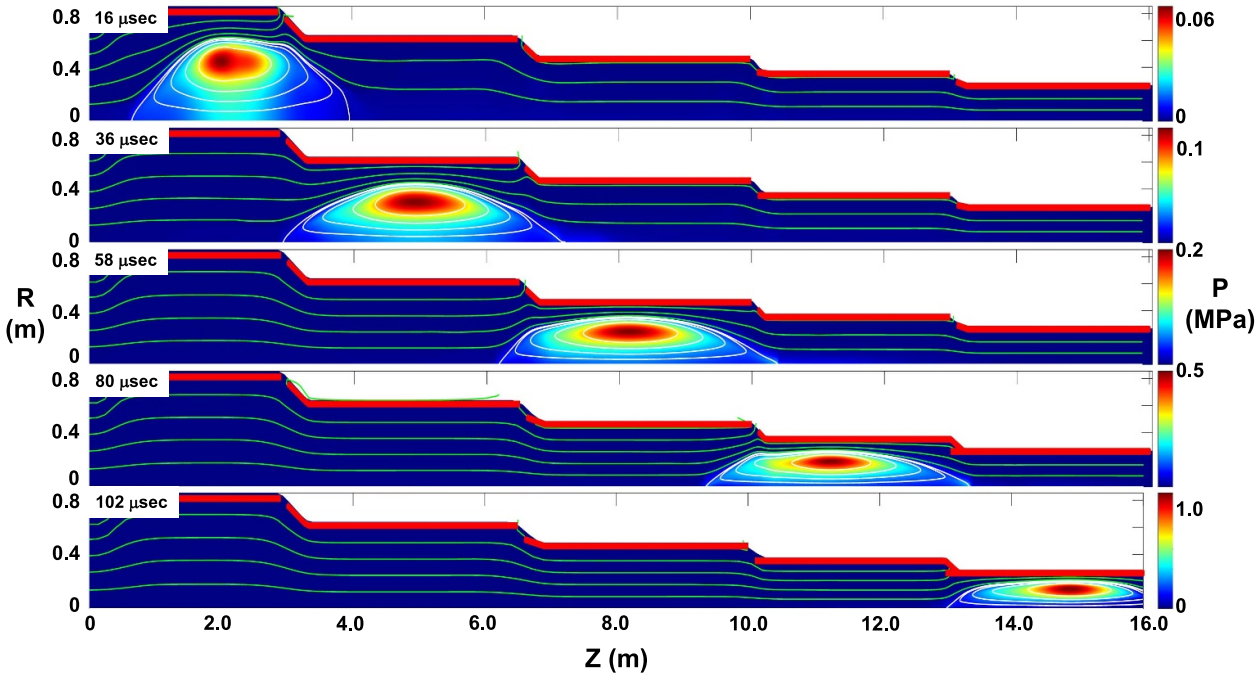

Figure 19. Pressure contours and field line plots from the 2D resistive MHD calculation at various times during first five stages for the adiabatic wall compression of the FRC of the Compact FRC Fusion Reactor (CFR2) concept.

considerably less dissipation and reflect the plasma-based LHD resistivity employed in the code. The pronounced initial decay reflects the s resistivity as the value of s/ε exceeds one. This continues until the flux diminishes and the ions reach a temperature sufficient for stability at around 25 μs.

Maintaining the roughly 130 km s^{-1} drift for all nine stages, the 26 m can be traversed in roughly 200 μs. Assuming the anticipated 5 ms flux decay time, the flux on entry into the final stage (burn chamber) would thus be essentially unchanged ($\varphi_p{}^f/\varphi_p{}^i = 0.96$) Even with the significantly lower τ_φ from

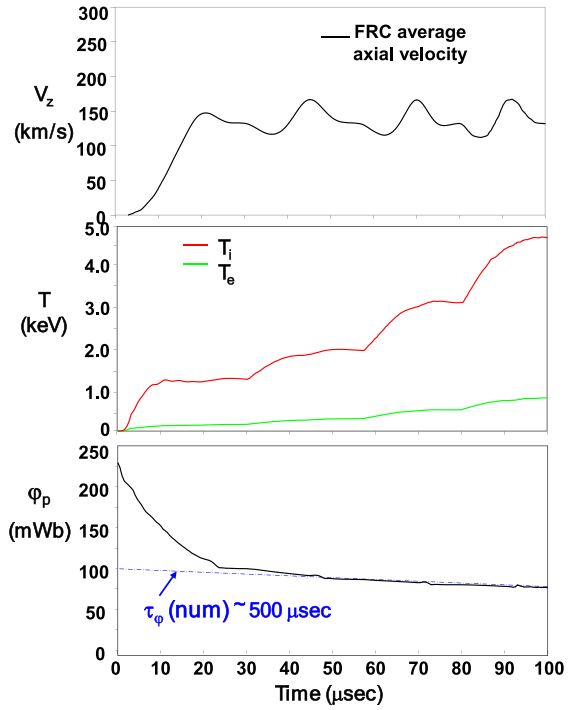

Figure 20. Temporal plots from the calculation shown in figure 19 for various key parameters.

the much higher code resistivity, the final flux would still be 60 mWb. From figure 6, the FRC would be able to achieve a fusion gain of five at 30 T, providing sufficient margin if one encounters flux loss rates greater than the scaling prediction based on the observed FRC stationary equilibrium rate.

4.2. FRC flux compression verses wall compression

At this point it is reasonable to consider whether simply compressing the FRC to fusion conditions with one or possibly two coils (formation and a compressor) would achieve the same parameters as the CFR2. Essentially, this would involve a single coil flux compression to attain the same fusion plasma. However, this approach is problematic for several reasons. One issue, as has been remarked on earlier, is that flux compression increases the FRC average beta with the consequent increase in the separatrix density making transport losses even higher. Another problem is the energy required would be enormous. Starting with a 0.8 m compression coil 4 m in length (the size of the FRC formation coil in CFR2), the stored energy to reach a field of 30 T would be nearly 3 GJ.

In a pulsed magnetic fusion system, there are several elements of the driver circuit where ohmic losses can be minimized for the delivery and return of the stored energy, usually by massive parallelization of the switches, cable etc. There are, however, fundamental losses associated with magnetic diffusion into the coils themselves. If one assumes that the compression coil is to be energized on the same timescale as the CFR2 wall compression, and then recovered back into the storage (capacitor) bank, one has $T/2 = 400$ μs where T is the period

Wall compression: $\varphi_p(x_s)$ **is constant**	**Flux compression:** $\varphi_p(r_c)$ **is constant**
$\varphi_p \sim r_s^2 B_e$	$\varphi_p \sim x_s^3 B_e$
$B_e \sim r_s^{-2}$	$B_e \sim x_s^{-3}$
$T_i \sim B_e^{4/5} \sim r_s^{-8/5}$	$T_i \sim x_s^{-12/5} \langle\beta\rangle^{2/5}$
$s \sim r_s^{-1} T_i^{-1/2}$	$s \sim x_s^{-1} T_i^{-1/2}$
$s \sim r_s^{-1/5}$	$s \sim x_s^{1/5} \langle\beta\rangle^{-1/5}$
$\varepsilon \sim l_s r_s^{-1}$	$\varepsilon \sim l_s x_s^{-1}$
$l_s \sim r_s^{2/5}$	$l_s \sim x_s^{8/5} \langle\beta\rangle^{3/5}$
$\varepsilon \sim r_s^{-3/5}$	$\varepsilon \sim x_s^{3/5} \langle\beta\rangle^{3/5}$
$s/\varepsilon \sim r_s^{2/5}$	$s/\varepsilon \sim r_s^{-2/5} \langle\beta\rangle^{-4/5}$

Figure 21. Adiabatic scaling laws for $\gamma = 5/3$ for wall compression and flux compression of the FRC for key plasma parameters. A rigid rotor profile was assumed for the poloidal flux.

for a full oscillation. The ohmic losses in the compression coil is given by equation (12),

$$E_\Omega = \frac{B^2}{2\mu_0} A_{\text{wall}}\, s_e, \tag{12}$$

where A_{wall} is the coil inner wall area and s_ε is the energy skin depth and is equal to 1.27δ. Here δ, is the weighted flux skin-depth for the half cycle considered here [39]:

$$\delta = 0.803 \left(\frac{\eta}{\mu_0} \frac{T}{2} \right)^{1/2}. \tag{13}$$

It will be assumed that the coil is constructed from the same Beryllium copper alloy that could be used as the first wall for the CFR2 reactor as it possesses one of the highest tensile strengths and is an excellent conductor as well (50% that of pure copper). Given this and the other stated parameters, the flux compression coil would dissipate 25 MJ of energy per pulse.

As will be seen, the FRC thermal energy at stage 10 in CFR2 is roughly 3.6 MJ at a compression field of 35 T. Consequently, flux compression at this scale would thus be far too lossy. In fact, any reliance on flux compression is counter-productive as it is not only more dissipative, but can also be destabilizing as will be seen in the next subsection.

4.2.1. FRC parametric scaling and stability. Once formed and heated by flux dissipation, the FRC is observed to be stable and the plasma well confined as long as the plasma remains within a kinetic regime where $s/\varepsilon < 1$. It is essential to examine how flux and wall compression affect the basic FRC plasma parameters with regard to this stability condition. The scaling of key parameters for an elongated FRC under both flux and wall compression have been elucidated in previous analytic work [40], and are stated in figure 21. Also found in figure 21 is the scaling for the stability condition implied by the parameter scaling. The stability condition for wall compression scales favorably; as the FRC is compressed, the s/ε value for the FRC

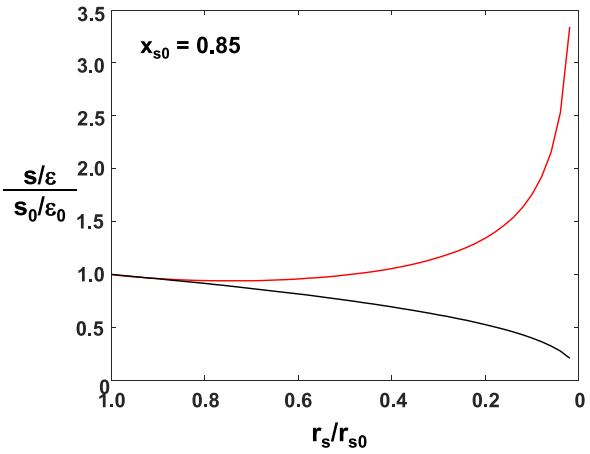

Figure 22. Change in the stability parameter normalized to the initial value at $x_s = 0.85$ for adiabatic wall compression (black) and flux compression (red) as a function of radius normalized to the initial radius.

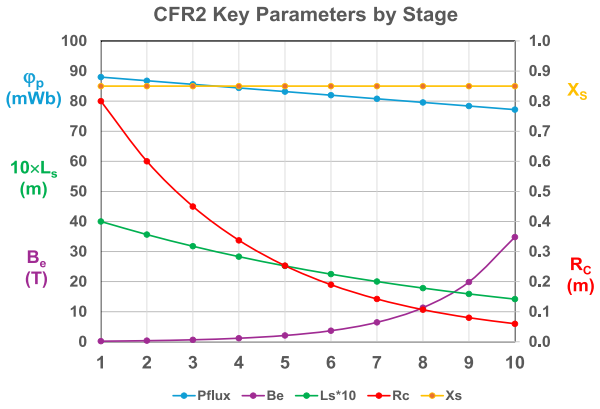

Figure 23. Key FRC fusion scaling parameters at each stage of the adiabatic wall compression in CFR2. The final stage is that of the burn chamber.

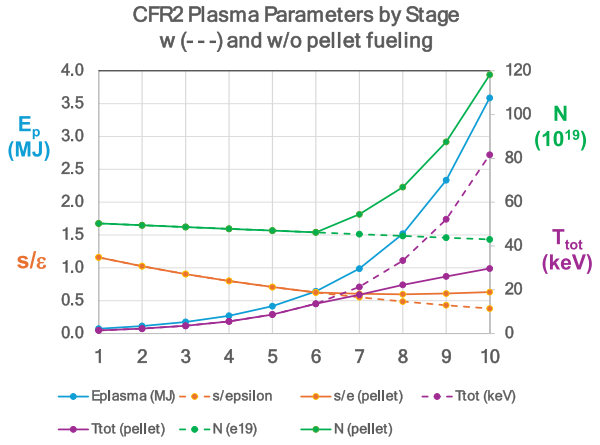

Figure 24. Key FRC plasma parameters at each stage of the CFR2 with and without additional pellet fuelling. The final stage is that of the burn chamber.

is reduced. On the other hand, flux compression has a negative scaling so that as one compresses the FRC the stability deteriorates. The stability condition variation with compression is shown graphically in figure 22. Here the initial x_s value of 0.85 for the FRC is assumed for both wall and flux compression cases. It is also assumed that the FRC starts at the limit where $s/\varepsilon = 1$. Initially the flux compression case decreases in a manner similar to the wall compression as the average beta increases with flux compression. Even though energy transport is significantly increased by this trend, it is initially stabilizing. Once the average beta begins to saturate near unity, the negative radius scaling prevails as the contracting FRC elongation begins to dominate. The opposite is the case for wall compression. Having a much lower s/ε for the final stages of the CFR2 turns out to be very advantageous as will be discussed in the next section.

4.2.2. CFR2 staged wall compression scaling. The 2D resistive MHD numerical calculations for the formation and staged compression discussed earlier in section 4.1 served as the basis for the scale, timing, and manner of operation for producing a suitable fusion grade FRC. Due to the limitations of code related losses, an analytical approach was employed to determine more precisely the plasma parameters at each stage. The adiabatic scaling laws for wall compression were assumed along with the initial FRC equilibrium parameters and velocity maintained through each stage from the code results shown in figures 19 and 20. It is anticipated that the equilibrium flux and particle loss scaling from past *in situ* experiments would be applicable here. However, a more conservative approach was adopted by assuming the confinement was decreased by a factor of three from the empirical *in-situ* scaling stated in equation (3). The more cautious value provides for a significant margin of error, accounting for potential deviations in confinement from past results. Despite the increased losses, this approach still enables the target parameters for FRC reactor burn shown in figure 6 to be achieved. Results of the analysis for key parameters at each stage of compression of the FRC can be found in figures 23 and 24.

It should be noted that the compression target values of at least a 30 T confining field and a minimum FRC poloidal flux of 60 mWb are exceeded even with the assumption of reduced flux and particle confinement. To maximize flux retention, it is critical to achieve kinetic stability as early as possible. The starting equilibrium temperature needs to be relatively high. From the 2D code calculations shown in figure 20, the initial plasma temperature after formation is ∼1.4 keV.

While stabilizing, a consequence of the high initial plasma temperature is that the staged wall compression of this plasma would yield a plasma temperature greater than 80 keV as indicated in figure 24. This is considerably higher than desired for fusion gain as the fusion cross section increases more slowly than $T_i^{5/2}$ above $T_i \sim 15$ keV (see figure 5). Moreover, the high T_i is not required for stability as evidenced in figure 24. The optimal solution involves increasing the plasma density at the expense of temperature. This is accomplished with pellet fueling which will be examined next.

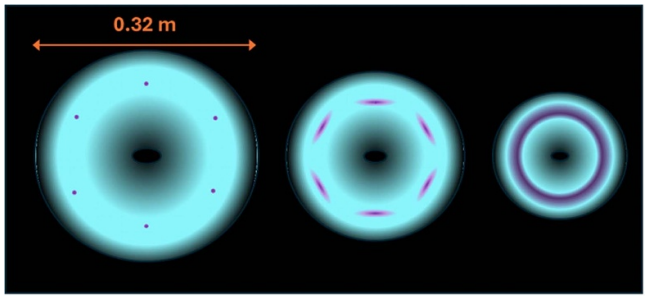

Figure 25. Scheme for pellet fueling on CFR2 as would appear end-on. DT pellets are dropped at six ports and fall in the vertical direction. They are timed to arrive at the positions uniformly about the axis of symmetry as shown which corresponds to the FRC null radius at stage 6 and onward.

4.2.3. CFR2 pellet fueling during the later stages. The pellet injection can be readily accomplished in the CFR2 as it does not require a high velocity pellet injector as the drifting FRC provides a stationary pellet with a relative velocity of more than 130 km s^{-1}. The pellets can be inserted from ports at various distances along the latter stages. The stability parameter s/ε has sufficiently decreased by that point so as to not be destabilized by the subsequent slower rise in ion temperature as the density is increased. The total energy gained by compression at each stage is unchanged. As indicated in figure 24 it can be seen that the target plasma temperature of 30 keV for the final stage burn would require the particle inventory to increase by roughly a factor of three. Figure 25 provides an end-on illustration of the process for 6 pellets inserted in the sixth stage.

The total frozen D–T pellet total volume required, assuming an average atomic mass of 2.5, is $V_{\rm tot} \sim 18$ mm^3. This can be supplied by 6–18 pellets depending on ablation rates as well as the stage at insertion. Stage 6 was nominally chosen as the stability parameter at this point has dropped to $s/\varepsilon = 0.6$. The size, location and number of pellets would be determined so that the rate of ionization would produce the increase in inventory shown in figure 24. This has the effect of holding s/ε roughly constant through the remaining stages. While some of the parameters of figure 24 change substantially due to the increase in plasma inventory, the parameters shown in figure 23 do not. This is due to the fact that the energy loss from dissociation and ionization, roughly 50 eV per D–T neutral, is only 3.2 kJ. This is negligible compared to the total FRC energy gained from compression of 3.6 MJ.

It will require further study and experimentation to determine the best application of pellets as the peak plasma density changes significantly from stage 6 (2.5×10^{21} m^{-3}) to stage 9 (2×10^{22} m^{-3}). The FRC, however, remains highly elongated (2.3 m $> l_s >$ 1.6 m), so there should be more than enough distance and density for the pellet to be rapidly ablated and ionized in the FRC null region. Plasma production here is expected to significantly increase τ_N by at least $n^{1/2}$ (see equation (3)), and possibly more as was found in tokamak pellet injection experiments [41]. The flux confinement is also expected to increase as was found in neutral beam sustained FRCs [10]. This positive behavior would not be unexpected. The creation of plasma near the null is in the most magnetically confined region of the FRC. With the buildup of new plasma, the diffusion outward of the plasma tends to flatten the magnetic gradient by opposing the inward diffusion of the FRC magnetic flux, thereby also slowing the flux loss in the process as well.

4.3. Fusion burn stage in the CFR2

The final stage for the translating FRC is the reactor burn chamber. The flux compression here, as it is in all the previous stages, is performed by the FRC as it passes into the low magnetic bias field of the next chamber and excludes this vacuum bias flux to the region external to the FRC. As mentioned earlier, with wall compression the bias flux is the same for all stages as it is in the 2D MHD calculations in figure 19. However, as the FRC flux decreases slightly from stage to stage, so must the bias flux in order to maintain the x_s at a constant value of 0.85.

From figure 23 the remaining poloidal flux by stage 10 is 77 mWb. To maintain the x_s at 0.85, an external field of 34.8 T is necessary for the 6 cm inner conducting wall radius of the burn chamber. The required bias magnetic field is given by $B_e{\cdot}(1-{x_s}^2) = 9.65$ T. From figures 23 and 24 along with equation (8*b*)), the fusion gain for this FRC plasma is determined to be 9.1.

Unlike the previous stages where a dielectric vacuum boundary is required to achieve the plasma radius reduction for insertion into the next stage coil, there is no need for further active compression. The chamber wall can thus be the conducting boundary for the confinement of the magnetic flux. The length of this chamber is considerably longer in order to position the FRC for optimal interception of the neutron flux for both energy gain and Tritium breeding. With the FRC centered in the burn chamber, less than 0.2% of the fusion neutrons would escape without significant interaction with the burn chamber and only about 2% would avoid complete thermalization in the surrounding blanket. The burn chamber axial layout without the surrounding blanket was indicated figure 18. A more detailed cross-sectional drawing can be found in figure 26. Here it can be seen that the quasi-steady bias field is produced by a series of multiturn solenoids constructed from Be_2Al alloy which has an ultimate yield strength of 440 MPa, equivalent to the magnetic pressure of 33 T. It also has excellent conductivity at 50% that of copper. The inner beryllium copper (BeCu) cylinder bears the transient magnetic pressure from the FRC compression, while the Be_2Al solenoid is subjected only to the pressure from the axial bias field (<10 T). The number density of beryllium is over 80% of the alloy making it a highly effective material for neutron multiplication.

The use of FLiBe as the fusion blanket material for cooling and Tritium breeding has many advantages in this application. FLiBe has a low neutron absorption cross-section, high volumetric heat capacity [42], and is liquid in the temperature range 732–1703 K [43]. In particular, for the CFR2 configuration illustrated in figure 26, the high resistivity of FLiBe

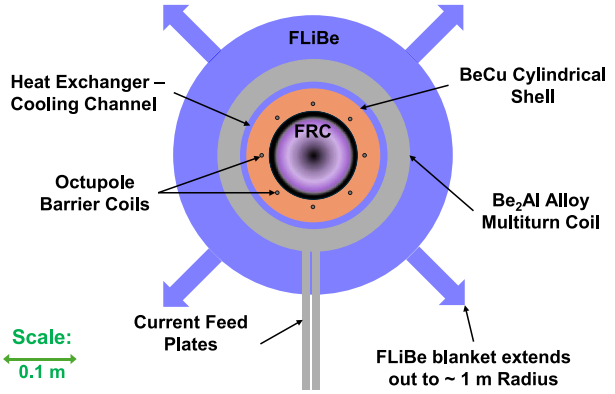

Figure 26. Cross sectional schematic of the main elements of the CFR2 burn chamber.

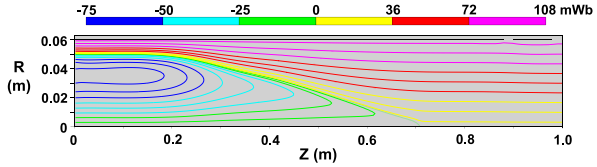

Figure 27. Magnetic flux lines from the 2D resistive MHD code for the FRC equilibrium in the burn chamber with the parameters shown in figures 23 and 24 for stage 10.

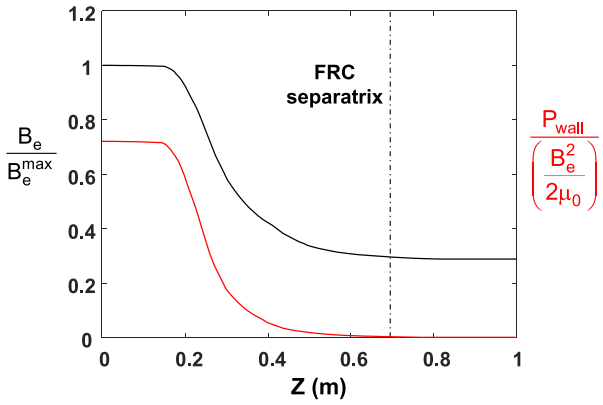

Figure 28. The normalized axial magnetic field along the burn chamber wall from the calculation shown in figure 27 (black). The radial magnetic pressure at the wall induced by the FRC flux exclusion normalized to the pressure that would be inferred by the total axial magnetic field.

($\sim 10^6 \times$ Cu) greatly simplifies the insulation and operation of the Be_2Al solenoids as well as providing a cooling channel for direct cooling of the inner flux-conserving cylindrical shell as well. The CFR2 reactor geometry and high volumetric coverage provides for efficient neutron multiplication and thermalization, potentially providing a tritium breeding multiplier as high as 2.

The BeCu serves as both the flux conserving conductor as well as the first wall of the burn chamber. It is well suited for this task as there are BeCu alloys that have ultimate tensile strengths as high as 1.5 GPa (equivalent to 61.4 T) with a conductivity up to 33% of copper. Wall materials such as tungsten could also be used but would lack the Be multiplier. Another first wall possibility is extruded beryllium tubing which typically has an ultimate tensile strength between 690 and 830 MPa, thus making it also an excellent choice for the plasma-facing first wall.

It should be noted that for FRC parameters considered here, the extent of the high magnetic field at the wall is considerably less than the FRC length. From the 2D code, the equilibrium shape was determined for the highly elongated burn chamber FRC ($\varepsilon \sim 14$). The FRC axial and radial profile of the magnetic flux is found in figure 27. The magnitude of the axial magnetic field along the inner wall of the flux conserver is shown in figure 28. The Lorentz or hoop force acting on the wall currents is less what would be inferred from the total magnetic field at the wall of 34.8 T. This is due to the fact that the 9.7 T bias field produced by the outer solenoidal coils has time to penetrate the inner cylinder so that at the time of FRC insertion there are no currents flowing in the chamber wall. As can be seen from figure 28, the magnetic pressure at the wall from the FRC compression is (320 MPa) is 0.72 that implied by the full field. It can also be seen that this high-pressure region extends only over a fraction of the FRC length ($\sim$20%).

The FRC motion through the burn chamber is controlled primarily by the magnitude of the bias flux along the axis of the burn chamber. It was found in the staged compression MHD calculations that small changes in the bias flux can significantly accelerate or decelerate the FRC. On entrance into the stage 10 burn chamber the characteristic velocity of the FRC maintained throughout the previous stages ($\sim$135 km s^{-1}) is reduced but maintained by a small axial gradient in the bias flux until the FRC reaches the middle section of the burn chamber. Here the bias flux is slightly increased to reduce the drift velocity to around 10 km s^{-1} contingent on the confinement time of the FRC. If the confinement exceeds that predicted by equation (3) a slower drift and/or a longer burn chamber would be in order. The FRC drifts over the central meter with the high field central region the FRC spanning 0.3 m. The skin depth given by equations (12) is thus reduced by roughly a factor of two and the local wall heating by a factor of 4. From equation (13) The ohmic losses during the central burn are less than 60 kJ which is negligible compared to the fusion energy gain.

An important consideration during the burn phase is the retention and capture of the 3.5 MeV fusion alphas. The D and T ions are considerably higher in temperature at the start of the burn, but electron–ion equilibration balance the temperatures on a timescale $\tau_{ex} \sim 0.6$ ms. This process will be accelerated by the presence of the alphas. The alphas also heat the plasma maintaining and even increasing their temperature even though the poloidal flux decay leads to a decrease in the external magnetic field. This heating therefore also allows for an initially higher plasma density enhancing both confinement and fusion yield. The alphas will have significantly larger gyro-orbits which aid FRC stability.

The question arises as to whether these ^{4}He ions are confined by the FRC at the large x_s values needed to minimize thermal plasma losses at the separatrix. To address this question the orbits of the alphas were calculated for an FRC

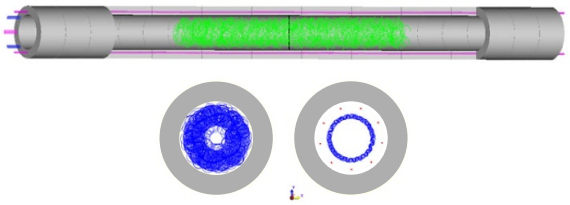

Figure 29. (Top) Cutaway showing 300 3.5 MeV alpha ion orbits in a FRC with a RR flux profile for $x_s = 0.85$ and $B_e = 27$ T. Five of the eight barrier rods, as well as burn chamber flux conserving coils are shown. (Bottom left) end-on view of the alpha orbits. (Bottom right). 10 keV D ion orbits at the null and near the separatrix are shown for comparison.

with a RR profile and an $x_s = 0.85$ with an external field of 34 T characteristic of the initial FRC insertion as well as at 27 T representing conditions at mid burn. The monoenergetic 3.5 MeV alphas were launched isotropically with the number emitted at each location weighted by the density squared (see equation (3). Given the peaked density at high x_s (see figure 3), the number of alpha emitters, 3000 in all, were highly concentrated near the null as would be the case in the FRC burn. The result from the calculation can be found in figure 29 where the orbits for 300 of these alpha ions are shown. It was determined that were no alphas lost at 34 T. The number increased below 32 T, eventually rising to roughly 5% at 27 T with the alphas either striking the wall or escaping. The application of the barrier fields, produced by the axial current rods illustrated in the top figure of figure 29, at a level needed to keep the FRC centered and rotationally stable, made no significant effect on the alpha confinement due to their relative weakness compared to the external axial magnetic field. It should be noted that screening currents at the FRC separatrix prevent barrier field penetration into the FRC which also limits their influence on the alpha orbits.

After a few milliseconds the FRC is beginning to leave the central section of the burn chamber. Up to this point the bias field has been tapering off so as to maintain the x_s roughly constant as the FRC poloidal flux decays. This in turn has led to a lowered compression field and consequently fusion gain. Minimizing flux-loss is critical to fusion gain since it not only causes a direct reduction in the gain, flux-loss decreases the FRC radius. Since the coil flux remains constant, B_e decreases, which reduces the gain even more.

Given the sensitivity of fusion gain to both confining field and FRC flux (see equation (8)), it became apparent that to evaluate the overall fusion gain, a time-dependent model of the key FRC parameters was required. Such a calculation was carried out that followed the evolution of the FRC in the burn chamber. The temporal evolution of the fusion relevant parameters is shown in figure 30. The resultant fusion energy output (equation (4)) and plasma energy decay inferred for the FRC with the high x_s scaling (equation (3)), as well as other FRC parameters are found in figure 31.

It should be noted that there are important changes in the vacuum magnetic field bias, B_0, axially along the burn chamber during the initial FRC burn. Due to the wall acting as a

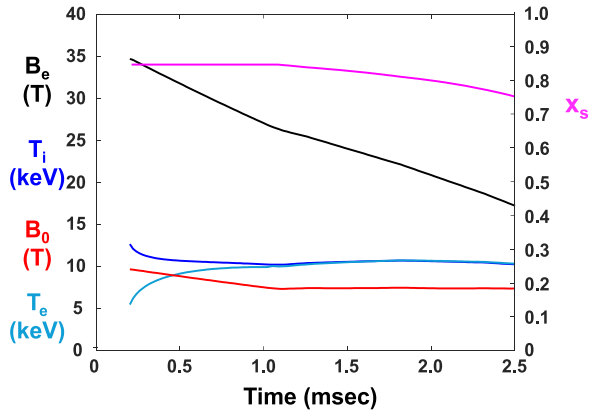

Figure 30. Various FRC parameters during the fusion burn. The FRC enters the burn chamber at 200 microseconds.

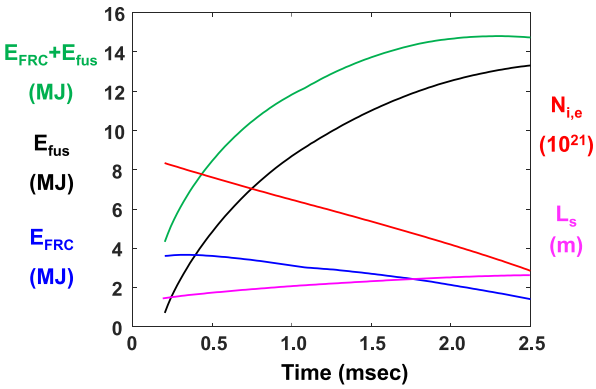

Figure 31. Temporal evolution of key energy and plasma parameters during the fusion burn in CFR2.

flux conserver on this time scale, the change in B_0 experienced by the FRC sustains the drifting into a different section of the burn chamber cylinder. The initial drop-off in bias flux is made to maintain the FRC at an x_s of 0.85. The consequent axial gradient also aids in quickly moving the FRC toward the center of the burn chamber. As mentioned, at external magnetic fields below 27 T the fusion alphas begin to be lost to the walls. At this juncture the vacuum flux, $B_0 \pi r_w^2$, is kept at roughly 7.5 T as this vacuum flux, which becomes the external flux to the FRC as the FRC passes, keeps the alphas well confined to the FRC even though the external field continues to decrease from FRC flux loss. It also allows for the slow drift of the FRC to continue for the remaining fusion burn. From figure 30 this transition occurs at roughly 800 us into the burn. Another consequence of the roughly constant B_0 is that x_s must also decrease as the FRC flux decays. It can also be observed in figure 30 that the decrease is not large, and the x_s stays in a range where the separatrix plasma pressure to still remains low. From equation (3) the FRC confinement however continues to scale strongly with x_s so that the plasma flux confinement time, which was assumed to scale in a manner similar to the particle confinement, also experiences a reduction of roughly a factor of two over the remaining burn time due to the drop in x_s.

In the derivation of the fusion gain for high x_s FRCs it was assumed that $T_e = T_i$. This is certainly not the case after the initial formation where $f_T = T_e/T_i = 0.2$, a value that is typical for past FRTP formed FRCs. During the subsequent compression stages f_T rises to 0.42, still far from unity. Considering this more favorable division of temperature, a greater initial density in the burn chamber from pellet fueling during compression can be attained that puts the ion temperature in the optimal range at the start of the burn as indicated in figure 30. Correcting equation (6) for $f_T < 1$, the initial fusion gain of 9.1 is now increased by a factor of $[2/(1 + f_T)]^{5/2} = 2.35$ to over 21. As can be seen in figure 30, this enhancement quickly disappears due to energy exchange with both the D–T ions as well as the rapidly increasing alpha ion population which heats primarily the electrons.

While alpha heating maintains the plasma temperature despite a decreasing magnetic field pressure, it also adversely affects gain due to the immediate increase in the total thermal energy content of the FRC. It should be noted that an increase in the internal energy of the FRC does not result in an increase in plasma radius when confined in a constant, uniform flux conserver as it is here. Only an increase in poloidal flux can cause a radial increase. Flux-loss does increase the FRC length as the loss decreases the magnetic tension inside the FRC. Thus, both the alpha heating and flux-loss cause the FRC to grow in length as is readily attested to in figure 31. This is despite the particle loss which would cause a decrease in length. As indicated in figure 30, the alpha energy maintains the FRC ion and electron temperatures. This also causes the particle density to decrease along with decreasing B_e. and increasing length. As one would expect, all these effects have a significant impact on fusion energy generation as it scales as $n^{5/2}$ (see equation (5)).

Also, from figures 30 and 31, it is clear that there are significant changes in many of the key FRC and fusion parameters during the FRC burn. It is therefore imperative for any concept that is based on pulsed FRC fusion to develop a time dependent model when evaluating the ultimate fusion gain of the system. The evolution and decay of the FRC makes for profound changes in the fusion yield compared to simple calculations based on just assuming the initial reactor conditions. This consideration is particularly important for aneutronic fusion reactions. The impact on plasma density due to the plasma thermal expansion from fusion product ion heating would be much more severe than what was found here for D–T alphas. The fact that the required confinement times are orders of magnitude greater than D–T only acerbates the problem. FRC fusion based on D-^{3}He and P-^{11}B would expand at a far greater rate as all the fusion energy becomes FRC internal plasma energy. The rapid expansion substantially reduces the plasma density and in the process quenches fusion energy production.

The decay of the particle inventory, $N_{i,e}$, and thus FRC thermal energy is primarily due to convective particle loss. Thermal conduction losses for the FRC are typically much less significant. This is due to the rapid, convective plasma loss on the open divertor field lines, which essentially make the FRC vacuum isolated from chamber boundaries. The decline in particle inventory eventually accelerates as the confinement time decreases as $r_s{}^3 n^{1/2}$. Both terms contribute to the decrease τ_N, primarily from the radial dependence due to flux loss. The similar parametric dependence found empirically between τ_N and τ_φ [4] and assumed here, may be largely influenced by the significant drop in pressure across the separatrix at low x_s.

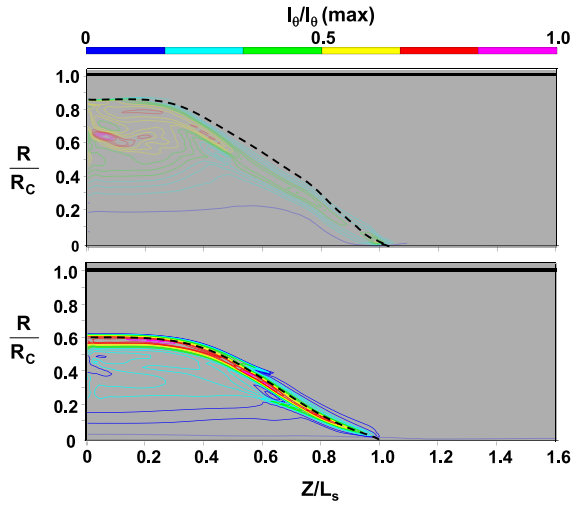

Figure 32. Normalized equilibrium θ current contours from 2D resistive MHD code for an equilibrium FRC at $x_s = 0.85$ (top) and $x_s = 0.6$ (bottom). Black dashed lines indicate the position of the FRC separatrix.

Virtually all the past experimental data predominately pertains to FRCs where flux compression yielded equilibrium x_s values of less than 0.6. As was pointed out earlier (see figure 3), the modification in pressure profiles at large x_s dramatically lowers the separatrix pressure and hence particle and energy loss. A steep, turbulent gradient at the separatrix edge will likely still persist for any practical value of x_s which suggests that an LHD-like scaling would also continue to persist, but with a much lower coefficient as was assumed here. The scenario for flux confinement, however, could be much different for the high x_s FRC. It should be reiterated that the confining poloidal flux of the FRC is due to diamagnetic currents and these currents predominantly flow where the pressure gradient is most pronounced. Comparing where the actual azimuthal or theta currents flow in the FRC at moderate and high x_s is illuminating.

The results of resistive 2D MHD calculations for the two cases can be found in figure 32. Notably, even at $x_s = 0.6$, the peak currents flow primarily in the separatrix region and decrease to a fraction of this at the FRC null. It is not surprising that the resistivity at the edge would be anomalous exhibiting a flux confinement similar to the anomalous particle confinement. The θ current for the high x_s case on the other hand shows a peak near the null radius with a much broader distribution. The flux scaling could thus be quite different and likely more favorable with the currents flowing primarily in a region of low turbulence than the particle confinement. The picture of a turbulent edge with a more quiescent interior is also supported by fluctuation measurements on the TAE C-2W experiments [44].

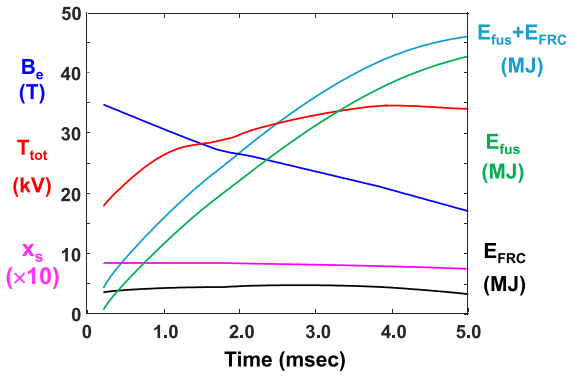

Figure 33. Temporal evolution of key energy and plasma parameters with improved τ_φ during the fusion burn in CFR2.

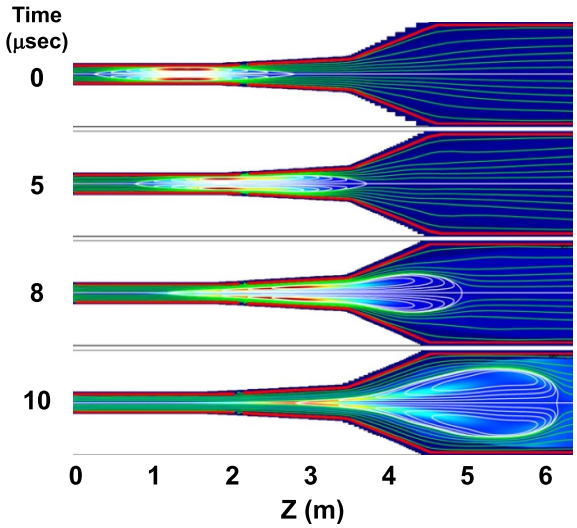

Figure 34. Pressure contours and field line plots at various times from a 2D MHD calculation of the FRC ejection from the CFR2 burn chamber into a much larger chamber with a much lower bias magnetic field.

The strong dependence on x_s and r_s will likely remain similar to that for τ_N (see equation (3)) as theses sensitivities reflect the general transport over the entire FRC. The density dependence in equation (3), however, relates more to the LHD effects of the edge turbulence and not the broader conditions surrounding the null where at high x_s the current is primarily located. The scaling with elongation is not as clear. It is likely related to the increased plasma density on the open, diverter field near the separatrix as the source delivering plasma onto the open field lines increases with elongation.

Eliminating both these terms from the τ_φ scaling results in an increase of a factor of 1.2 in the flux confinement time during the fusion burn. The primary cause driving the density reduction is due to plasma expansion from flux loss and alpha heating, both of which increase the elongation. A more significant improvement in τ_φ (by a factor 2.5) when the density dependence is eliminated. Seeking a middle ground, it was decided to examine the effects of a twofold improvement in τ_φ but assuming the same, more negative scaling dependencies as used for τ_N before. As expected, even though there is no change in the initial fusion gain, it persists for a longer period of time as key plasma, field, and fusion parameters in figure 33 attest.

A consequence of the prolonged high fusion gain was a rapid increase in the plasma temperature. To maintain the FRC temperature in the optimal range for fusion gain (<30 keV), pellet fueling was initiated at roughly 600 us. This would be accomplished as before by inserting small, frozen D–T pellets along the reactor length so as to be positioned at the FRC null radius and various azimuthal locations in a manner similar to method employed during the during the staged compression as in figure 25. These pellets are ingested by the FRC as it drifts along the burn chamber now with a relative injection velocity of 10–20 km s^{-1}. While pellet fueling helps maintain plasma density and temperature, the fusion gain, though optimized, continues to decline as FRC flux and plasma pressure, still decay over time.

The results displayed in figure 33 illustrate the sensitivity of the final fusion energy gain on the flux confinement. The final fusion gain is increased by a factor of 3.3 to approximately 12 even with the same negative particle confinement scaling. While encouraging, determination of the appropriate scaling awaits further experimental investigation of high temperature and density FRC plasmas at high x_s.

Given that the remaining FRC energy can be recovered with reasonable electrical efficiency, extending the burn phase beyond the range depicted in figure 33, and even somewhat earlier for the lower flux confinement case shown in figure 31, would offer minimal benefit.

At this point in the burn then, the FRC is moved rapidly out of the burn chamber coil into what will be referred to as the Energy Recovery Chamber (ERC). The ejection could be accomplished by a reduction in the axial bias magnetic field strength near the end of the burn chamber. However, given that the FRC still has an x_s of 0.75 an FRC expansion would bring the FRC perilously close to the inner burn chamber wall. Fusion continues to occur which would cause a large fraction of the fusion alphas to strike the inner wall. A more effective and less deleterious course is to progressively flare the end of the burn chamber coils out in radius and forming a conically shaped end coil. This allows the bias flux to remain high protecting the inner wall as well as increasing the ejection velocity. A 2D MHD calculation depicting this process can be found in figure 34.

The energetics and scaling of the electrical recovery process, along with its implementation methodology, will be addressed in the next section.

4.4. FRC divertor and energy recovery in CFR2

The final element of stage 10 involves the insertion of the FRC into a large chamber similar to that shown in figure 18. This chamber and coils are at a scale similar in size to the formation stage 1 coil set, but shorter in length and with a set of mirror coils to both stop and trap the ejected FRC. This chamber is

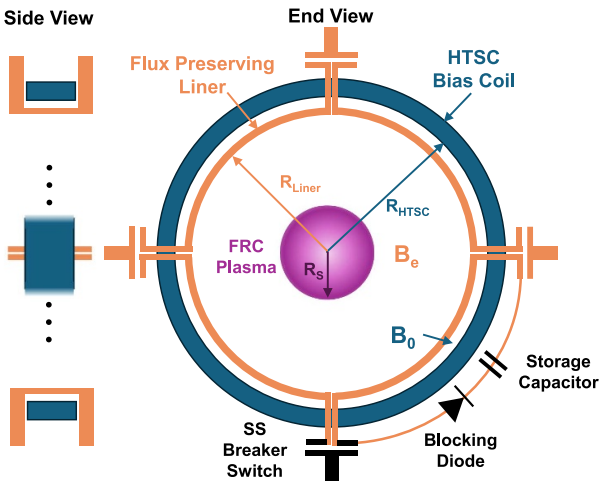

Figure 35. A schematic of an ERC coil with encompassing liner and recovery circuitry.

not dissimilar in function to that used in past FRC experiments such as the one discussed in section 3.2.1 and depicted in figures 9–12. Here however, the expansion chamber to burn chamber radius ratio is much larger (14:1). The reason for such a large ratio is that it provides for greater expansion which lowers the bias magnetic field required as well as the plasma energy density. Since the FRC will be allowed to decay in the ERC, the lowered plasma energy will help mitigate any more damage to where the diverted field terminates on the ERC wall.

For the efficiency analysis it will be assumed that the preexisting bias field, B_0, is provided by a high temperature super conducting (HTSC) coil to avoid any ohmic losses from a pulsed system on this scale. This is possible here given the minimal fusion output and the relatively low bias field requirement (~2 T). The induced currents in the flux preserving 'liner' coils are driven by the compression of the bias flux from FRC insertion and expansion. The liner coils are positioned radially inside and along the axial and radial extent of each of the HTSC coils. A schematic of one of these coils can be found in figure 35 along with other recovery elements to be explained shortly.

First a brief analysis of physics of energy recovery and parameter scaling will be given. The conversion of plasma energy into electrical energy is achieved through the FRC performing compressional work on the bias field as it enters and expands inside the ERC. Similar to the process discussed with regard to the burn chamber, the FRC compresses the preexisting magnetic field, produced by the external HTSC coils, inside the flux conserving liner shell to a final peak magnetic field B_e. The primary distinction in this context is that the FRC is constrained to remain stationary inside the chamber by mirror fields, and at much lower x_s.

One can equate the final thermal energy and work done by the FRC in terms of the initial FRC plasma energy, $E^i{}_{\rm FRC}$, after ejection form the burn chamber:

$$E^i_{\rm FRC} = E^f_{\rm FRC} + W_{\rm B}, \tag{14}$$

where the work done can be expressed as follows:

$$W_{\rm B} = \Delta E_{\rm B} = \left(\frac{B_e^2}{2\mu_0}\left(1-x_s^2\right) - \frac{B_0^2}{2\mu_0}\right) V_{\rm liner}$$
$$= \left(1-x_s^2\right) x_s^2 \frac{B_e^2}{2\mu_0} V_{\rm liner}. \tag{15}$$

where $B_0 = (1-{x_s}^2)B_e$ and $V_{\rm liner} = \pi {R_{\rm liner}}^2 l_{\rm liner}$. It is assumed here that l_s, the final equilibrium FRC length, is roughly the same as $l_{\rm liner}$, which is the length of the large radius, flux-conserving liner section between the mirror coils of the ERC. Thus, the final FRC volume is given by $V_{\rm FRC} = {x_s}^2\, V_{\rm liner}$. The final FRC energy, $E^f{}_{\rm FRC}$ can then be expressed as:

$$E^f_{\rm FRC} = \frac{3}{2}\frac{B_e^2}{2\mu_0} V_{\rm FRC} = \frac{3}{2} x_s^2 \frac{B_e^2}{2\mu_0} V_{\rm liner} = \frac{3}{2}\frac{1}{1-x_s^2} W_{\rm B}, \tag{16}$$

where equation (15) was used to restate the final FRC energy in terms of the work done in compressing the bias field by the FRC.

By substituting $E^f{}_{\rm FRC}$ from equation (16) in equation (14) one has:

$$E^i_{\rm FRC} = W_{\rm B}\left(1 + \frac{1.5}{1-x_s^2}\right) = W_{\rm B}\left(\frac{2.5-x_s^2}{1-x_s^2}\right). \tag{17}$$

The conversion efficiency, η, can therefore be expressed as:

$$\eta = \frac{W_{\rm B}}{E^i_{\rm FRC}} = \frac{1-x_s^2}{2.5-x_s^2}. \tag{18}$$

One can now solve for B_e and B_0 $[=(1-{x_s}^2)\cdot B_e]$ as a function of the initial FRC energy:

$$B_e = \left(\frac{2\mu_0}{V_{\rm coil}}\frac{E_{\rm B}}{1-x_s^2}\right)^{1/2} = \left(\frac{2\mu_0}{V_{\rm coil}}\frac{\eta E_{\rm FRC}}{1-x_s^2}\right)^{1/2}$$
$$B_e = \left(\frac{2\mu_0}{V_{\rm coil}}\frac{E_{\rm FRC}}{1+0.5x_s^2}\right)^{1/2}. \tag{19}$$

A plot of the efficiency, η, as a function of x_s is found in figure 36 along with the inferred bias and external fields for a nominal initial FRC energy of 2 MJ inserted into an ERC with a liner radius of 0.82 m and a length of 1.2 m can be found in figure 36. To obtain an efficiency of 38% an $x_s = 0.33$ would be required.

From equation (19) for $x_s = 0.33$ in the ERC and the FRC energy and particle inventory at the exit to the burn chamber, the equilibrium FRC parameters can be calculated assuming no significant losses in the FRC insertion and relaxation processes. With $B_e = 2.76$ T, along with equation (16), the FRC length would be 1.2 m in a constant flux coil. On that basis, it should also be the appropriate liner section length. Given the FRC inventory at the exit from the burn chamber, the particle density in the ERC chamber is $n = 1.45 \times 10^{21}$ m^{-3}. From pressure balance, $T_{\rm tot} = 13.1$ keV, and the confinement time from equation (2) is 810 μs.

The final step is to recover the work done in increasing the magnetic field potential energy inside the conducting liner

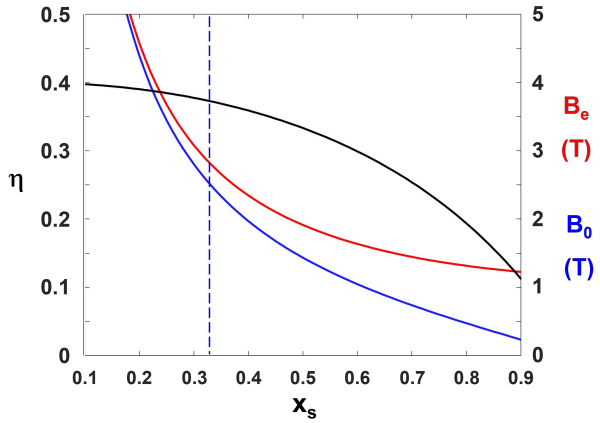

Figure 36. The energy recovery efficiency, η, as a function of the equilibrium FRC x_s in the ERC chamber as well as the initial bias magnetic field, B_0, and final external magnetic field B_e after FRC insertion. Dashed line indicates the x_s (0.33) at which $\eta = 0.38$.

by FRC compression. This is equal to the total current I_{liner} induced in the liner coils times the flux inside the liner coil:

$$W_{\text{B}} = \frac{1}{2}\phi_0 I_{\text{liner}} \tag{20}$$

where the flux is given by the initial vacuum flux inside the liner: $\phi_0 = \pi {R_{\text{liner}}}^2 B_0$, and remains constant throughout the process as on this timescale the liners continue to act as a flux conserver. The liner current however increases from zero to a maximum with the FRC achieving equilibrium inside the ERC. From Amperes law one has:

$$I_{\text{liner}} = \frac{l_{\text{liner}}}{\mu_0}\left(B_e - B_0\right) = \frac{l_{\text{liner}}}{\mu_0} B_e x_s^2 \tag{21}$$

where again the relation: $B_0 = (1 - {x_s}^2)\cdot B_e$ was used. As a check, substituting this expression along with that for ϕ_0 into equation (20)

$$W_{\text{B}} = \frac{1}{2}\pi R_{\text{liner}}^2 B_0 \frac{l_{\text{liner}}}{\mu_0} B_e x_s^2 = \left(1 - x_s^2\right) x_s^2 \frac{B_e^2}{2\mu_0} V_{\text{liner}}. \tag{22}$$

It can be seen that this recovers the same result as that of equation (15) confirming that the work done by FRC in compressing the ERC bias flux is equivalent to the energy flowing in the circuit. The storage of this energy into a capacitor is fairly straight forward.

The necessary circuit elements are illustrated in figure 35 in the lower left corner for one of the four sections that comprise the flux conserving liner. With the FRC at the maximum B_e and thus current, the solid-state breaker switches that were closed during current build up are opened. This occurs at roughly zero voltage across the switch and the current is shunted into the capacitor as the blocking diode now goes into conduction. The capacitor then charges storing the electrical energy until the current reaches zero. In the case shown in figure 35, the set of four circuits together then store all the energy due to the work performed by the FRC compression minus minimal circuit losses.

The division of the liner into sections is somewhat arbitrary. The more sections, the lower the fraction of the total charge accumulated on each capacitor and hence the final voltage that each capacitor and diode will experience. The charge time, as well as voltage, is determined by the size of the capacitance. The charging time should be kept short when compared to the FRC lifetime.

It is worth mentioning that the efficiency of conversion of FRC thermal energy into electrical is similar to what one would likely obtain from the conversion of the fusion neutron energy produced during burn. It has been assumed in the past that aneutronic FRC reactors could do much better than the maximum 40% conversion efficiency determined in this analysis. It stems from the notion that the FRC plasma behaves more or less as a free expansion both radially and axially as it is ejected into the relatively low field chamber. Due to the plasma kinetic energy, the plasma would continue to expand and compress the external flux until the plasma kinetic energy was exhausted. While this may occur transiently with a purely kinetic ionized gas, the actual process with an FRC is far from this description as the UW experimental results and numerical calculations depicted in figures 8–11 attest.

Here the FRC transited the confinement chamber with little expansion, and was subsequently compressed to high temperature at stagnation in the mirror throat (see figure 11). As indicated by the sustained high temperature, the FRC clearly retained much of this increase in internal energy into the equilibrium phase after the rebound. In this instance the increase in FRC energy came from converting the kinetic energy acquired in the accelerator, but the same subsequent dynamics would occur for the energy coming from fusion products. The retention of the bulk of the FRC total energy as internal energy is necessary in order to maintain radial and axial equilibrium with the internal magnetic field tension from the FRC poloidal flux. To have otherwise would cause the FRC to contract until this was the case. This energy is therefore not available to do compressional work other than what is allowed consistent with a balance with the internal magnetic field tension. As determined in the foregoing analysis, this is never greater than 40% of the total energy prior to FRC expansion.

5. Conclusion and discussion

5.1. Summary of the CFR2 concept

A new methodology for achieving the formation and compressional heating of a FRC plasmoid to reach fusion gain has been elucidated. At each step of the process, theoretical analysis, resistive 2D calculations, particle orbit analysis, and past experimental evidence were presented that justify the methodology and conclusions. This includes experimental work at the University of Washington and MSNW that had not been previously reported which supports key elements of high x_s formation and translation. In addition, robust recovery from non-adiabatic FRC injection into a large chamber has been demonstrated.

The particle and flux lifetimes based on previous FRC empirical (LSX) scaling was updated to include recent FRC

experimental results. Based on the stability parameter scaling, as well as the final stability results from LSX, the staged compression of the FRC can be done in such a manner as to maintain the FRC stability from formation throughout the fusion burn. It was found that timely fueling of the FRC during the compression and burn phases provides a means to maintain the FRC at the optimum ion temperature of 15 keV during the burn phase. Analysis based on the FRC confinement scaling found that the fusion gain for the FRC, G, is proportional to $\varphi_p \cdot {B_e}^2$ where φ_p is the FRC poloidal flux and B_e the confining axial magnetic field. G is essentially independent of the FRC size making feasible a small, compact reactor with a high ratio of surface to reacting volume. In addition, the remaining nondimensional scaling factors for fusion gain, x_s and elongation, ε, were optimized. The x_s was maintained at the largest practical value throughout ($x_s = 0.85$) and the elongation maximized by the staged wall compression process ending with $\varepsilon \sim 14$, both of which brought the expected fusion gain to near 10. Two key elements for attaining high fusion gain were the lower transport losses at high x_s and high flux retention ($\varphi_p > 80$ mWb) accomplished by employing a non-aggressive form of dynamic FRC formation in a large ($r_w \sim 0.8$ m), elongated chamber ($l_c \sim 4$ m) with the high initial ion temperature ($T_i > 1$ keV) necessary for stability and reduced flux loss.

The essential components of the staged compression method for achieving high fusion gain are a combination of high ion temperature, a steady FRC translation at subsonic velocity (10–15 km s^{-1}), along with small incremental radius reductions employing adiabatic and isentropic radial compression only. This method does appear to preclude the approach previously proposed by the author where supersonic merging was employed for compression and heating. However, this approach avoids the catastrophic flux loss that occurs during the simultaneous acceleration and compression phase, as well as the adverse aspects of flux compression of the resultant merged FRCs to reach fusion temperatures. Also, with the CFR2 being a single-ended device, it makes possible a travelling fusion burn minimizing first wall thermal loading issues. With no need for flux compression in the burn chamber, a much more robust first wall can be employed providing for a close-fitting flux conserver at the maximum confining fields. It also provides a straightforward way to recover some of the remnant energy from the FRC in a remote chamber at termination.

5.2. Discussion

As with any new concept there are more unanswered questions than answered. A short list of the latter would include the technologies that need to be developed to achieve a functional reactor. Fortunately, the ability to construct and test the concept can be accomplished with existing technologies as it would require nothing more than what has been used in prior FRC experiments at MSNW, Helion Energy and TAE. A significant future challenge will involve producing a repetitive pulsed system and determining the optimum rep rate as these will ultimately determine the electrical output from fusion power. The primary challenge for repetitive pulsing is the development of high-power solid-state circuitry. Given the rapid progress in this branch of electronics, it is anticipated that this goal can most likely be met. A detailed overview of the technology needed for a steady-state, repetitively pulsed CFR2 will be presented in another publication. Plans for ongoing development and potential solutions to key challenges will also be presented.

Another important and related question is the maximum thermal wall loading. It is commonly assumed that 10 MW m^{-2} is the upper limit for a tokamak reactor. This is based on the essentially permanent first wall and a stationary plasma. However, the situation for the CFR2 reactor is considerably different. As mentioned, the CFR2 has one of the highest surface-to-wall ratios. Moreover, the FRC is not a stationary object. The wall surface area that is exposed to the neutron flux can be adjusted by simply increasing the length of the CFR2 burn chamber.

For the optimal scenario depicted in figure 33 for the CFR2, out of the 43 MJ of fusion energy generated 27 MJ was in the form of 14.1 MeV neutrons that pass through the first wall. A relatively slow drift of the FRC of 1 km s^{-1} would have the FRC travel 5 m during the 5 ms burn. This would expose the reactor wall to roughly 14 MJ m^{-2}. It is worth noting that the power experienced at the wall is determined by the pulse repetition rate. The wall loading can therefore be further reduced by decreasing the pulse rep rate to slightly over one second for the case considered here. It can also be accomplished by a slightly faster FRC drift speed and a longer burn chamber. Higher loading is also a possibility as the burn chamber wall is readily replaceable. Wall loading is thus not a serious issue for the CFR2 concept.

It should be noted that the CFR2 concept still includes the advantage of the natural divertor of the open field lines surrounding the FRC. The radius of the FRC is closer to the wall in CFR2 than previous experiments due to the much greater internal poloidal flux. There is still, however, ample flux external to the FRC to provide a conduit for plasma lost from the FRC to be diverted to the end chambers before diffusing radially to the reactor wall. As it is in other fusion reactors such as the ITER tokamak, the SOL radial extent is miniscule as the radial diffusion rate is a tiny fraction of the sonic outflow velocity along the divertor flux. For ITER it is predicted to be on the order of 1 mm. The density scale length of the SOL observed for the FRC is roughly an ion gyro radius which for the reactor stage FRC is the radial extent is roughly 0.6 mm for a 10 keV ion (see figure 29). It is expected that the edge ion temperature will be significantly less than this which shrinks the radial extent even further. The high fields attained between the FRC and reactor wall will also suppress any impurity ions emitted from the wall from traversing the roughly 1 cm gap between the FRC and the wall. As it is a traveling FRC burn, any neutrals released from the reactor wall will not have sufficient time to reach the FRC as it passes.

There is one final, and fundamental aspect of FRC physics to be addressed, and it pertains to constraints defining the operational boundaries for the FRC as a fusion plasma. There are obvious technological constraints such as strength of materials, power handling and durability of solid-state devices, etc.

These limitations can be addressed by further improvements in current performance as outlined above. The primary focus here is on the intrinsic limitations posed by the transport and stability characteristics inherent to the FRC.

The analysis of CFR2 parameters described in section 4 originated from a specific set of conditions for the initial FRC formation size, fields, fill pressure, voltage etc. Due to the increase in radial scale needed for greater FRC equilibrium flux, the primary requirement for determining many of the initial parameters was to quickly attain stability for the FRC to the many MHD modes that are endemic to the FRC when ρ_i/r_s is reduced. The final parameters that were desired for the fusion burn stage were determined essentially by employing a point design approach. This approach assured adherence to what had been demonstrated in the past. Given the FRC susceptibility to the internal tilt being the most critical, it was paramount to make sure that the stability criterion was satisfied throughout the formation, compression and burn stages. It is important to understand the implications this constraint may impose on any changes in scale, elongation, magnetic fields etc. from the point design.

As indicated by equation (9), increasing the radial scale for greater FRC flux results in the stability criterion becoming a limiting constraint. Restating the stability criterion using equation (9), one has:

$$1 \geqslant \frac{s}{\varepsilon} = 1.52 \times 10^3 \frac{\varphi_p}{\varepsilon r_s \sqrt{A_i T_i}} = 1.52 \times 10^3 \frac{r_c x_s^2 B_e}{\varepsilon \sqrt{A_i T_i}}, \quad (23)$$

where a RR profile was assumed for φ_p. This equation can be further simplified with the assumption of the optimum ion temperature (15 keV) and a balanced D–T mix ($A_i = 2.5$). Solving equation (23) then for the stability limitation on r_c:

$$0.1763 \frac{\varepsilon}{B_e} \geqslant r_c, \quad (24)$$

where the maximum reasonable value of $x_s = 0.85$ was also assumed.

One can now plot the maximum coil radius, R_{Cmax}, as a function of the external confining field for a given FRC elongation. The result is found in figure 37. With R_{Cmax} specified, one can determine a maximum poloidal flux $\varphi_{pmax} \cong x_s {r_s}^2 B_e = (0.85)^3 {R_{Cmax}}^2 B_e$. Also plotted on figure 37 are the results of equation (8) for fusion gain 5 and 10 for comparison purposes. The stability limit in poloidal flux and reactor coil radius is indicated by the transition from a solid line to a dashed one for $G = 5$ and 10 for an elongation of 15 which is similar to that obtained for the CFR2 point design. The limitation on coil radius for a fusion gain $G = 10$ occurs at $R_{Cmax} = 0.114$ m. This is slightly less than double that of the CFR2 point design. Even at $G = 5$ the coil radius cannot exceed 0.23 m. Given the decay in gain experienced in the time dependent calculations, an initial gain of at least 10 is likely to be needed to keep the CFR2 recirculated power reasonable. The operating space of CFR2 could thus be increased with a volume increase of $(0.114/0.06)^3 = 6.8$. This would be important if more fusion energy per pulse was desired. As was pointed out earlier, the fusion gain is independent of reactor scale.

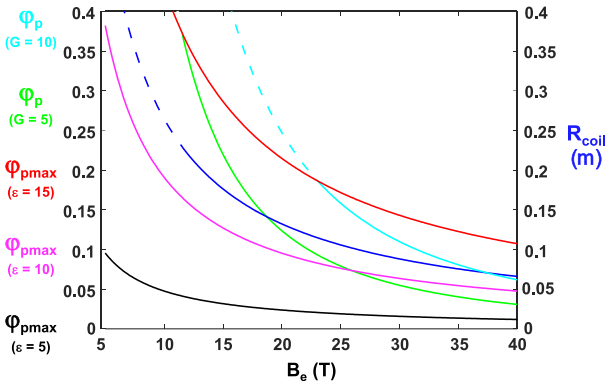

Figure 37. φ_p-B_e space for stable FRC equilibria for various FRC elongations in fusion burn stage. FRC stability is found only below curves for FRC elongations of 5, 10, and 15 with the curve indicating the maximum FRC flux. For all cases $x_s = 0.85$ and $T_i = 15$ keV. Also shown are the fusion gain curves for D–T at 5 and 10 as in figure 6.

The increase in scale would allow for more reactor flux. From the graph, FRC flux could increase to a maximum of 200 mWb at a gain of 10 and allow for operation at a lower B_e (23 T). The increase in flux however would need to be accompanied with a larger and longer staged compression section.

It should be noted that FRC elongation plays a large role here. For an elongation of 10 the point design for the CFR2 would be near the limit at $G = 5$ and would not reach 10 without external fields greater than 40 T. At an elongation of 5, there is no operational space for the FRC to achieve even a gain of 5.

It should also be noted that it is unlikely that the stability issue would be a problem for FRCs created by neutral beam injection due to the subpopulation of large orbit ions as in the recent TAE experiments [9]. However, a great impediment to this approach is the diamagnetic nature of the FRC poloidal field currents. It is not particularly surprising that producing a suitably high-pressure plasma annulus from beam heating would create a field reversal and form an FRC. The problem is that this diamagnetic current is likely to, and did, exhibit the anomalous resistivity characteristic of the high β FRC. The FRC generation in these experiments required 6 MW of beam power to form and sustain an FRC with roughly a thermal energy of 2.35 kJ for an energy confinement time on the order of 400 μs. Given the large background plasma helping to mitigate the separatrix density gradient, this confinement time is not that different from the 300 μs predicted by equation (2). The resistive anomaly however is still quite large as the Spitzer perpendicular resistivity for the 315 eV electron temperature reported would predict a $\tau_\varphi = 56$ ms. With a B_e of only 0.11 T, the resulting Lawson parameter for this neutral beam generated FRC is 6×10^{15} m^{-3} keV s, which over four orders of magnitude less than what is needed for D–T fusion breakeven let alone gain. The 6 MW of neutral beam power is already as large or larger than that employed by the largest tokamaks for heating and current drive that already reach near breakeven conditions. This leaves little room for improvement of the sort necessary to reach ignition in D–T let alone P-^{11}B.

There is however the possibility of employing the neutral beams as part of the initial FRC formation stage in CFR2. Enhancing the stability of the FRC would be a good way to widen the operating regime for the FRC as the stability limit is quite restrictive. As such, it must be a part of the formation phase as it must be present as all stages of the FRC compression process. Fortunately, this is also quite feasible during the first stage of the CFR2 as it is of sufficient size and would not complicate the reactor operation. It is likely that this could expand the stable operational region for FRC fusion and possibly improve flux retention and confinement as well.

Given the unique nature of the FRC plasma with great potential advantages for fusion but at the same time clear limitations, it is hoped that the CFR2 as described here has threaded this needle. It is at least an approach that is feasible.

References

[1] Armstrong W.T., Linford R.K., Lipson J., Platts D.A. and Sherwood E.G. 1981 *Phys. Fluids* **24** 2068
[2] Tuszewski M. 1988 *Nucl. Fusion* **28** 2033
[3] Tuszewski M., Barnes D.C., Rej D.J. and Taggart D.P. 1991 *Phys. Fluids B* **3** 2205
[4] Hoffman A.L. and Slough J.T. 1993 *Nucl. Fusion* **33** 27
[5] Slough J.T., Hoffman A.L., Milroy R.D., Crawford E.A., Cecik M., Maqueda R., Wurden G.A., Ito Y. and Shiokawa A. 1992 *Phys. Rev. Lett.* **69** 2212
[6] Slough J.T., Hoffman A.L., Milroy R.D., Maqueda R. and Steinhauer L.C. 1995 *Phys. Plasmas* **2** 2286
[7] Slough J.T., Votroubek G. and Pihl C. 2011 *Nucl. Fusion* **51** 053008
[8] Tuszewski M. *et al* 2012 *Phys. Rev. Lett.* **108** 255008
[9] Roche A. *et al* 2025 *Nat. Commun.* **16** 3487
[10] Gota H. *et al* 2024 *Nucl. Fusion* **64** 112014
[11] Asai T. *et al* 2024 *Nucl. Fusion* **64** 096013
[12] McKenna K.F. 1983 *Phys. Rev. Lett.* **50** 1787
[13] Slough J.T., Hoffman A.L., Milroy R.D., Harding D.G. and Steinhauer L.C. 1984 *Nucl. Fusion* **24** 1537
[14] Hoffman A.L. and Slough J.T. 1986 *Nucl. Fusion* **26** 1693
[15] Rej D.J., Taggart D.P., Baron M.H., Chrien R.E., Gribble R.J., Tuszewski M., Waganaar W.J. and Wright B.L. 1992 *Phys. Fluids B* **4** 1909
[16] Momota H., Ishida A., Kohzaki Y., Miley G.H., Ohi S., Ohnishi M., Sato K., Steinhauer L.C., Tomita Y. and Tuszewski M. 1992 *Fusion Technol.* **21** 2307
[17] Slough J.T. *et al* 2022 *U.S. Patent US* 11,469,003 B2
[18] Steinhauer L.C. 2011 *Phys. Plasmas* **18** 070501
[19] Rosenbluth M.N. *et al* 1962 *Nucl. Fusion Suppl.* **Pt. 1** 143
[20] Post R.F. 1987 *Nucl. Fusion* **27** 1577
[21] Milroy R.D. and Slough J.T. 1987 *Phys. Fluids* **30** 3566
[22] Tuszewski M. 1988 *Phys. Fluids* **31** 3754
[23] Slough J.T. and Milroy R.D. 1989 *Phys. Fluids B* **1** 840
[24] Slough J.T. and Hoffman A.L. 1990 *Phys. Fluids B* **2** 797
[25] Rej D.J., Armstrong W.T., Chrien R.E., Klingner P.L., Linford R.K., McKenna K.F., Sherwood E.G., Siemon R.E., Tuszewski M. and Milroy R.D. 1986 *Phys. Fluids* **29** 852
[26] Tanjyo M. 1984 *Technol. Rep. Osaka Univ.* **34** 1759–81
[27] Ito Y., Tanjyo M., Ohi S., Goto S. and Ishimura T. 1987 *Phys. Fluids* **30** 168
[28] Slough J. and Votroubek G. 2006 *42nd AIAA/ASME/SAE/ASEE Joint Propulsion Conf.* AIAA2006-4654 (*Sacramento, CA, 9–12 July 2006*)
[29] Votroubek G., Slough J.T., Andreason S. and Pihl C. 2008 *J. Fusion Energy* **27** 123
[30] Binderbauer M.W. *et al* 2010 *Phys. Rev. Lett.* **105** 045003
[31] Gota H. 2019 *Nucl. Fusion* **59** 112009
[32] Slough J.T., Andreason S., Gota H., Pihl C. and Votroubek G. 2007 *J. Fusion Energy* **26** 199
[33] Slough J.T. and Milroy R.D. 2010 *J. Fusion Energy* **29** 567
[34] Tuszewski M., Taggart D.P., Chrien R.E., Rej D.J., Siemon R.E. and Wright B.L. 1991 *Phys. Fluids B* **3** 2856
[35] Slough J.T. and Hoffman A.L. 1993 *Phys. Fluids B* **5** 4386
[36] Brackbill J.U. and Saltzman J.S. 1982 *J. Comput. Phys.* **46** 342
[37] Milroy R.D. and Brackbill J.U. 1982 *Phys. Fluids* **25** 782
[38] Kirtley D.E. and Milroy R.D. 2023 *J. Fusion Energy* **42** 30
[39] Turchi P.J. 2025 *Phys. Plasmas* **32** 022507
[40] Spencer R.L., Tuszewski M. and Linford R.K. 1983 *Phys. Fluids* **26** 1564
[41] Milora S.L. *et al* 1980 *Nucl. Fusion* **20** 1491
[42] Übeyli M. 2003 *J. Fusion Energy* **22** 51
[43] Rodriguez A., Lam S. and Hu M. 2021 *ACS Appl. Mater. Int.* **13** 55367
[44] Thompson M.C., Schindler T.M., Mendoza R., Gota H., Putvinski S. and Binderbauer M.W. 2019 *Rev. Sci. Instrum.* **89** 10K114